Intense, Variable Mixing near the Head of Monterey Submarine Canyon

GLENN S. CARTER AND MICHAEL C. GREGG

Applied Physics Laboratory and School of Oceanography, University of Washington, Seattle, Washington

(Manuscript received 1 February 2002, in final form 25 April 2002)

ABSTRACT

A microstructure survey near the head of Monterey Submarine Canyon, the first in a canyon, confirmed earlier inferences that coastal submarine canyons are sites of intense mixing. The data collected during two weeks in August 1997 showed turbulent kinetic energy dissipation and diapycnal diffusivity up to 10^3 times higher than in the open ocean. Dissipation and diapycnal diffusivity within 10 km of the canyon head were among the highest observed anywhere ($\overline{\varepsilon} = 1.1 \times 10^{-6}$ W kg^{-1}; $\overline{K_\rho} = 1.0 \times 10^{-2}$ m^2 s^{-1}). Mixing occurred mainly in an on-axis stratified turbulent layer, with thickness and intensity increasing from neap to spring tide. Strain spectra showed a gentler than k_z^{-1} rolloff, suggesting that critical reflection and scattering may push energy into high wavenumbers. Dissipation dependence on shear appears to be much weaker in the canyon than in the open ocean, with indications that the dependence maybe as low as $\varepsilon \propto \sqrt{S}$. Coastal canyons may account for a small but significant fraction of the internal tide energy budget. A crude estimate of global dissipation in canyons is 58 GW, ≈15% of the estimated global M_2 internal tide dissipation.

1. Introduction

Coastal submarine canyons are widely expected to be sites of enhanced mixing. Theory along with limited observations suggest that internal wave energy is trapped and energy density increased by canyon topography. When internal waves reflect from solid boundaries, they preserve their angle relative to gravity (as opposed to relative to the reflecting surface). This can result in increased energy density because the distance between ray paths may decrease upon reflection. Three classes of reflection are possible depending on the ratio of bottom slope (b) to the slope of internal wave energy propagation (γ), defined as

$$\gamma = \frac{k_h}{k_z} = \frac{\lambda_z}{\lambda_h} = \sqrt{\frac{\omega^2 - f^2}{N^2 - \omega^2}}, \qquad (1)$$

where k, λ, and ω are the wavenumber, wavelength, and frequency of the internal wave (the z and h subscripts refer to vertical and horizontal directions, respectively); N is the buoyancy frequency; and f is the Coriolis frequency. For subcritical reflection, $b/\gamma < 1$, the internal waves are reflected into shallower water. For supercritical reflection, $b/\gamma > 1$, internal waves are reflected toward deeper water. At the critical angle, $b/\gamma \approx 1$, the linear theory has a singularity with nonlinear effects and turbulence dominating.

Focusing of internal waves, and hence increased energy density, toward the floor and head of a submarine canyon is expected from linear theory. The slope of the canyon floor is often less than critical for the M_2 internal tide, resulting in subcritical reflection and energy propagation towards the head. Typically, canyon sidewalls are steep, therefore internal wave energy entering the canyon from above is reflected down by supercritical reflection (Hotchkiss and Wunsch 1982; Gordon and Marshall 1976). Breaking internal waves dissipate their energy through turbulence. Wave–wave and topography interactions, which cause internal waves to break, may be enhanced in a canyon.

Wunsch and Webb (1979) calculated normalized total energy density for near-bed current-meter deployments in and around Hydrographer Canyon. Their energy density values, corresponding to a 5-h period, showed an almost fivefold increase from the mouth of the canyon (depth 2106 m) into the canyon (depth 713 m). Two progressively shallower stations (512 and 348 m) showed the energy density decreasing to less than twice the level at the canyon mouth. They report that the shape of the frequency spectra remained nearly constant with changing energy density levels throughout the canyon. No comparison was made with the background open ocean Garrett–Munk (GM) spectrum.

Hotchkiss and Wunsch (1982) examined energy density in the internal wave frequency band from a moored temperature and current-meter array in Hudson Canyon.

Corresponding author address: Glenn S. Carter, Applied Physics Laboratory, University of Washington, 1013 NE 40th St., Seattle, WA 98105.
E-mail: carter@apl.washington.edu

© 2002 American Meteorological Society

They analyzed 14 temperature–pressure and six current-meter time series from five moorings. One mooring pair was 8 km from the canyon head (depth 350 m), a second pair was at 27–28 km (~780 m depth) and a single mooring was at 15 km (depth 500 m). Horizontal kinetic energy normalized by stratification was generally higher near the bed and at inshore moorings. Their normalized potential energy density calculations indicate an increase of 100 times toward the canyon head and up to 10 times from the top of a mooring to the bottom. In both kinetic and potential energy calculations there is some variation from this general trend.

When linear internal wave theory breaks down ($b/\gamma \approx 1$), one of the possible nonlinear effects are turbulent bores. Laboratory (Ivey and Nokes 1989) and numerical (Slinn and Riley 1996) studies have found that the nature of the bore evolves with number of wave cycles and depends of the steepness of the critical slope. Turbulent bores have been observed in submarine canyons using moored arrays (e.g., Gardner 1989; Key 1999).

2. Experiment

a. Previous studies in Monterey Bay

Monterey Canyon has bottom slopes ranging from 1.7° to 2.6° between depths from 1000 to 100 m (Rosenfeld et al. 1999). The average canyon axis slope within 10 km of the head is 2.1°. Measured sidewall slopes during a cross-canyon survey were 10.8° on the northern side and 15.7° on the southern. Petruncio et al. (1998) found that the M_2 internal tide, with a characteristic slope of ~2.3°, was dominant in Monterey Bay. Therefore, from linear theory, we expected energy density and dissipation to increase toward the head and the bed with some nonlinear effects such as tidal bores.

Lueck and Osborn (1985) found a high dissipation layer on the southern flank of Monterey Canyon in depths from 240 to 450 m, where the axial depth was 600 m. Over two days (3 December 1982 and 21 April 1983), they took nine profiles using expendable dissipation profilers. On the first day they found what they termed a turbulent bottom boundary layer, up to 170 m thick, and during the second day this layer's thickness was $\leq$50 m.[1] Within this turbulent bottom boundary layer, ε was $\leq 3 \times 10^{-6}$ W kg^{-1}, with $K_\rho \leq 15 \times 10^{-4}$ m^2 s^{-1}. Above the turbulent layer, the average dissipation rate was $<10^{-8}$ W kg^{-1}.

Petruncio et al. (1998) report that in Monterey Canyon the internal tide was best described as a progressive wave on one occasion and as an alongslope standing wave during a second experiment. They suggested that this was due to differences in the density field. In particular, increased stratification resulted in flatter characteristics and more reflections to give rise to the alongslope standing wave. Assuming that velocity and density vary sinusoidally over a tidal cycle, Petruncio et al. (1998) estimated internal tide energy fluxes at a pair of CTD/ADCP stations. They considered a boxlike canyon and that the changes in energy flux were due solely to dissipation, giving $\varepsilon = 1.3 \times 10^{-7}$ W kg^{-1}. Taking into account that the canyon cross-sectional area decreased toward the head, by approximately 8 times, $\varepsilon = 2.2 \times 10^{-6}$ W kg^{-1}. Dissipating all the energy flux from the shallower station along the remaining 3 km of the canyon axis would have required $\varepsilon = 1.6 \times 10^{-6}$ W kg^{-1}.

b. Measurements

Microstructure and internal wave surveys were conducted in the Monterey Submarine Canyon from 8 to 22 August (yeardays[2] 219–233) 1997. Using expendable current profilers (XCP) and CTD data, Kunze et al. (2002) found that internal waves in Monterey Canyon (offshore of the 500-m isobath) were almost an order of magnitude more energetic than the open ocean. The M_2 and its harmonic tides dominated with near-inertial motions absent. Horizontal energy fluxes were predominately up canyon and weaken from 5 kW m^{-1} at the mouth to <1 kW m^{-1} near the head, although both convergences and divergences existed. Kunze et al. (2002) found no evidence of focusing by sidewalls. Importantly, they suggest that interactions with canyon topography may transfer energy to small scales more efficiently than wave–wave interactions, resulting in fundamentally different turbulence production to the open ocean.

Evidence of tidal bores in Monterey Canyon during the period of the experiment was obtained using upward looking ADCPs and thermistors tethered 6 m above the bed (Key 1999). Cold water intrusions were observed on most tidal cycles. Large tilt values measured by the ADCP accelerometers were highly correlated with the most rapid temperature drops. The combination of high acceleration and a sudden drop in temperature were taken to indicate the front of a tidal bore passing. Tidal bores occurred less frequently than cold water intrusions.

The microstructure component (Fig. 1) was surveyed using the deep Advanced Microstructure Profiler (AMP), which has a maximum depth of 1500 m, and the newer Modular Microstructure Profiler (MMP), which has a maximum depth of 300 m. Both profilers measure the turbulent kinetic energy dissipation rate ε (Osborn and Crawford 1980; Wesson and Gregg 1994), temperature, and conductivity. Diapycnal diffusivity can be computed from

$$K_\rho = \frac{\Gamma \varepsilon}{N^2}, \tag{2}$$

[1] They give the height of the layer for drop 057 as 108 m (Table 2), but from the profiles, we suggest ~50 m and then there is a weaker midwater-column dissipation patch starting 25 m higher.

[2] Yearday is defined as decimal days elapsed since the beginning of the year (UTC); that is, noon on 1 January is yearday 0.5.

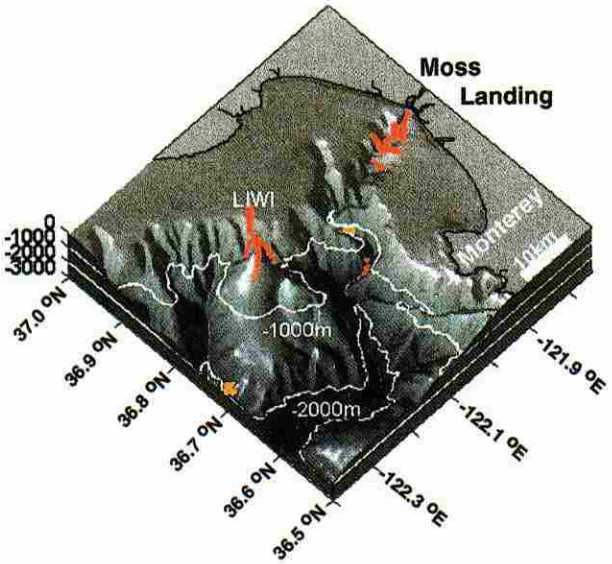

FIG. 1. Map of the Monterey Submarine Canyon. The location of microstructure drops are marked in red. Those on the submarine fan outside the bay are part of the Littoral Internal Wave Initiative (LIWI) and are described in Lien and Gregg (2001). The locations of the two MBARI moorings are indicated by orange squares. The inshore one (near the mouth of the bay) is M1 and the outer one is M2.

where Γ, the mixing efficiency, is taken to be ≤ 0.2 (Osborn 1980).

Most of the data were collected with the AMPs after the loss of an MMP instrument (recovered by the Monterey Bay Aquarium Research Institute after the experiment). Conductivities from the AMPs (Neil Brown sensors) drifted during the two-week experiment. Offset corrections were made by bootstrapping between conductivity measurements made with SeaBird sensors, using a technique similar to Bacon et al. (2001). A calibration error required that one of the AMP instruments have a linear slope correction applied to the conductivity.

Figure 2a shows the distribution in time and space of the microstructure measurements near the canyon head. The ship alternated between microstructure and internal wave surveys, resulting in approximately 12-h gaps between sets of AMP data. The 2.5-day gap (yeardays 224 to 226.5) resulted when measurements were taken out of the canyon as part of the Littoral Internal Wave Initiative (LIWI; Lien and Gregg 2001). The majority of the drops fell along the canyon axis within 10 km of Moss Landing. [The coordinate system used was distance in kilometers from the canyon head (Moss Landing) along the deepest part of the canyon axis. Although the canyon axis lies predominantly east–west, the direction can vary up to 90° meaning that canyon axis distance cannot be related to longitude.] These drops form two groups collected during neap and spring tides, with 111 and 212 drops, respectively. Over a 22-h period, 190 drops were made across the canyon 9.1 km from Moss Landing. An additional 28 drops were made in a region from 12 to 15 km from Moss Landing, where the canyon axis ran north–south rather than the predominant east–west direction.

A 150-kHz broadband vessel-mounted ADCP surveyed the water column from 11 m to ~260 m with 4-m vertical resolution. Its power supply failed at yearday 227 (0300), but data from a 150-kHz, vessel-mounted narrowband ADCP with 8-m vertical resolution was available after yearday 229. Surface tides recorded at Monterey Harbor as part of the National Oceanic and Atmospheric Administration (NOAA) National Water Level Observation Network (NWLON) were also used in the analysis.

c. *Environment*

Meteorological data were available from the R/V *Point Sur* and from long-term surface moorings. The Monterey Bay Aquarium Research Institute (MBARI) established and operates two moorings: M1 at the mouth of Monterey Bay (36.75°N, −122.03°E) and M2 offshore (36.70°N, −122.39°E). Mooring locations are marked as orange squares in Fig. 1.

Prior to the experiment (yearday 218), hourly-averaged wind vectors from the MBARI M2 mooring (Fig. 2a) measured strong equatorward (i.e., upwelling favorable) winds. Between yearday 219 and 222 the offshore winds reversed to become poleward. For the rest of the experiment, the offshore winds were mainly eastward with a weak equatorward component. Changes such as these in the wind field tend to be dominated by large scales (>500 km) (Hickey 1998). For example, similar patterns (upwelling winds followed by poleward then mainly eastward winds) were observed at the NOAA National Data Buoy Center mooring off San Francisco (Fig. 2a). Hourly averaged winds within Monterey Bay were of larger magnitude and more variable direction than those offshore. Wind gusts of up to 16 m s^{-1} were measured on board the R/V *Point Sur*.

The winds along the Californian coast are generally equatorward during summer (Hickey 1979, 1998). Figure 2b, daily averaged winds from the MBARI M2 mooring for summer 1997, shows mainly strong, southeastward, upwelling favorable winds. Relaxation events (weakening or reversal of equatorward winds) occur throughout the summer and generally last 2–3 days. The period of our experiment, shaded gray, is clearly not representative of summer wind conditions. This period is an unusually long relaxation event, taking approximately 10 days to resume consistent upwelling favorable winds, and contains the only day of northwestward winds during the 1997 summer.

Density profiles (Fig. 3) show three distinct states: the first 24 h of the neap survey, the remainder of the neap, and throughout spring. Changes in observed θ, s properties (Fig. 4) cannot be explained by mixing (e.g., after the first 24 h of the experiment, the top 40 m of

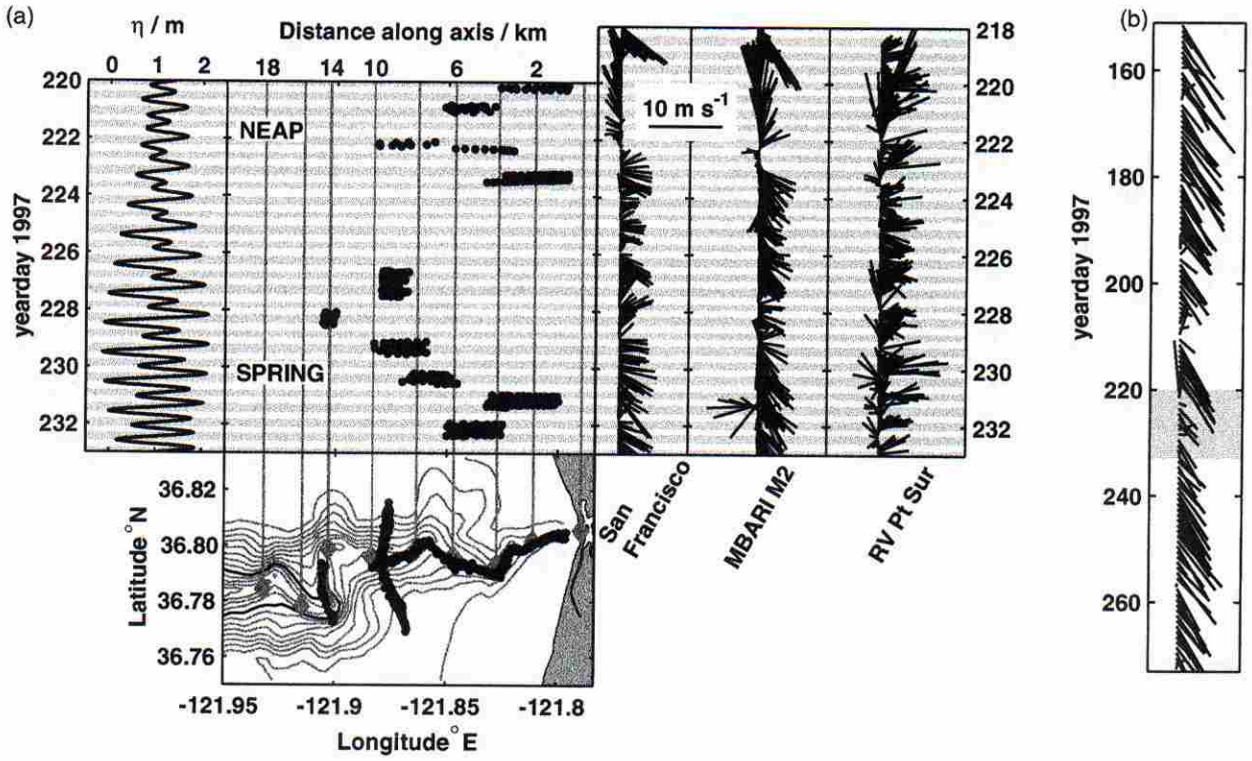

FIG. 2. (a) Location, in time and space, of microstructure drops near the canyon head (yearday 220 is 9 Aug). The horizontal shading marks the ebb tide, with reference to the surface elevation (η). Vertical lines mark distances along the canyon axis from Moss Landing, with the diamonds marking their location on the canyon axis. Fifty-meter contours are shown on the map with the darker line being the 500-m contour. The three right-hand panels show hourly wind vectors. From left to right, San Francisco (NOAA buoy), MBARI M2 (offshore mooring, Fig. 1), and local winds measured on the R/V *Point Sur*. The orientation of the vector gives the direction the wind is blowing toward (true north is up the page). (b) Daily averaged wind vectors from MBARI M2 mooring for summer (1 Jun–1 Oct) 1997. The gray region indicates the experiment period. The orientation and scale are the same as (a).

the water column becomes fresher), indicating the importance of advection.

1) NEAP UPWELL (YEARDAYS 220 0319–221 0125)

We have labeled the density structure during the first 24 h of the experiment as neap upwell, due to the location in the fortnightly tidal cycle and the presence of an upwelling signature. Near-surface θ, s observations were in qualitative agreement with previously studied coastal upwelled water within Monterey Bay. Rosenfeld et al. (1994) showed, using CTD and satellite SST data, that a tongue of cold water was advected into the euphotic zone after being upwelled at a coastal headland. The near-surface upwelled water that they observed was relatively cool (<10.5°C) and saline (>33.7 psu). The upper 40 m during the neap-upwell state had a salinity of approximately 33.7 psu with potential temperatures between 12° and 15°C (Fig. 4).

Drops >4 km from Moss Landing had a small near-surface density interface that eroded during ebb tide. The greatest variation, up to 0.5 kg m^{-3}, was below depth 150 m. Shallower drops (≤4 km), which were surveyed 12 h earlier, showed a more pronounced pycnocline that grew toward the head of the canyon. The strength of the pycnocline decreased toward high water. The average stratification was $\overline{N^2} = 6.6 \times 10^{-5}$ s^{-2}. Approximately 25% of the water column was between $11.5° \le \theta < 11.75$°C and $33.725 \le s < 33.75$ psu.

2) NEAP RELAX (YEARDAYS 222 0315–223 1215)

The remainder of the neap tide survey has been denoted neap relax as the cold, salty, upwelled water of the neap-upwell state completely disappeared over a period of less than 26 h. The main characteristic of neap relax was a sharp density interface ($\delta\rho \approx 1$ kg m^{-3}), which was observed in two locations and may represent an M_2 oscillation of approximately 60 m peak to peak. Petruncio et al. (1998) observed an internal tide of similar magnitude (70 m peak to peak). The average stratification was 7.5×10^{-5} s^{-2}.

At 10 km density increased 1 kg m^{-3} over 40 m across the pycnocline, and near the canyon head the interface sharpened to only 10 m thick. Above the interface was

a mixed region with properties between $13.5° \leq \theta < 15.3°C$ and $33.57 \leq s < 33.65$ psu, which became more homogeneous with increasing pycnocline depth and away from the canyon head. Below the pycnocline, density gradually increased to ~0.5 kg m^{-3} greater at the bed than the base of the pycnocline with properties falling between $8.9° \leq \theta < 10.5°C$ and $33.85 \leq s < 34.03$ psu. The water in the pycnocline fell on a straight mixing line between these two end points (Fig. 4). Pycnocline depth appeared to increase toward the head, but most of the bursts started at the onshore end, so this tilt may represent temporal change rather than spatial variability.

3) SPRING (YEARDAYS 227–233)

During spring tide (Fig. 3b), all drops between 5 and 10 km from Moss Landing had a similar shape: a surface mixed layer 10–20 m thick below which the density smoothly increased with depth. The variance was greatest above 200 m and was as large as 0.5 kg m^{-3}. Toward the head (≤5 km), the shape was less consistent because of increased variance (up to 1.25 kg m^{-3}) in the upper water column. The densest water occurred during early ebb and the lightest during early flood. The light water of early flood, particularly near the head, formed a pycnocline. The difference between surface and bottom density throughout spring tide was in excess of 2 kg m^{-3}. Average stratification was 6.9×10^{-5} s^{-2}. Although the θ, s curve (Fig. 4) passed through the two end points we observed during neap relax, the surface water was lighter, the deep water heavier, and the intermediate water more saline than would be expected from mixing.

During spring tide, the surface water density was 0.25–0.5 kg m^{-3} lighter than the surface water during neap. The bottom water was only slightly heavier during spring tide than neap. Within 4 km of the canyon head, the spring profiles were more variable and profiles taken during ebb (flood) were heavier (lighter) than those observed during neap. Individual profiles showed that the homogeneous bottom boundary layer was generally less than 15 m thick.

3. Observations: Monterey Canyon is an intense mixing location

a. Average profiles

All microstructure drops plotted in Fig. 2a have been used to give summary profiles, although the canyon cannot be considered either spatially homogeneous or in steady state. These 560 drops cover most of the canyon within 15 km of Moss Landing as well as a 22-h repeated cross-canyon survey. Observed dissipation ranged from 10^{-10} to $>10^{-4}$ W kg^{-1}, with $\bar{\varepsilon} = 1.1 \times 10^{-6}$ W kg^{-1}, and a 95% bootstrapped confidence interval on the mean of $[1.0 \times 10^{-6}–1.2 \times 10^{-6}]$ W kg^{-1}. Diapycnal diffusivity ranged from 7.0×10^{-8} to almost 10^{-1} m^2 s^{-1}, with $\overline{K_\rho} = 1.0 \times 10^{-2}$ m^2 s^{-1} ($[1.02 \times 10^{-2}–1.07 \times 10^{-2}]$ m^2 s^{-1}). Figure 5 shows profiles of ε, K_ρ, S^2, and N^2 averaged by depth and by height above the bed. Near-bed features are averaged throughout the water column in the depth average, but their relation to the bottom is preserved in the height average. Mixing occurred mainly in the lower water column (Figs. 6 and 9). Consequently, ε and K_ρ are best described in the height average. Shear and stratification, however, are best described by the depth average.

Depth-averaged stratification showed a nearly exponential decrease from $N^2 = 1.7 \times 10^{-4}$ s^{-2} at the surface to 1.2×10^{-5} s^{-2} at 450 m before increasing to N_0^2 near the bed ($N_0 = 0.0052$ s^{-1}). The increased stratification below 400 m was from 28 drops between 12 and 15 km, which were over 100 m deeper than those <10 km. Depth-averaged 8-m first difference shears decrease nearly exponentially from $S^2 = 6.8 \times 10^{-5}$ s^{-2} to $S^2 = 1.9 \times 10^{-5}$ s^{-2} at 260 m. In the upper 260 m, average 8-m shears were always less than stratification. The different slopes suggest that had deeper measurements of shear been possible, $S^2 \approx N^2$ may have been found in the lower water column, where mixing is strongest. Shear profiles from XCP data during the same period (Kunze et al. 2002) showed elevated shear levels in the lower water column, particularly as the canyon shoaled (500 < depth < 900 m).

Height averaging gave nearly constant stratification and shear profiles. This is entirely an artifact of the combination of N^2 and S^2 decaying from the surface and the sloping canyon floor. Near-bed values were dominated by the high values inshore of 3 km, while higher in the profile near-surface values dominated. Although height averaging N^2 and S^2 is in many ways misleading, two important points can be taken from it. Eight-meter S^2 values are less than N^2 values, in agreement with depth-averaging, which implies that at the measured depths and resolution there was no shear instability on average. Height averaging indicates that high dissipation can be associated with high stratification. Figure 6 shows this occurs mainly in shallow water.

Depth-averaged dissipation was fairly constant (~10^{-6} W kg^{-1}) from 150 to 350 m before dropping almost an order of magnitude at 400 m and then increasing toward the bed. The discontinuity, was from the 28 drops taken between 12 and 15 km. Height averaging was a better representation of the mean ε and K_ρ state because mixing generally occurred in stratified water above the sloping canyon floor (Figs. 6, 9, and 10). The height-averaged ε profile decreased from 2.8×10^{-6} W kg^{-1} at the bed to 10^{-7} W kg^{-1} at 400 mab (meters above bed). The K_ρ profile had a similar shape with a maximum value of 2.7×10^{-2} m^2 s^{-1} at 22 mab.

Both depth-averaged and height-averaged mixing profiles showed mid-water-column slope changes. In the depth-averaged plots, the change in slope occurred at ~180 m, which corresponds to $S^2 \approx N_0^2$ and stratification dropping to about a factor of 2 greater than shear.

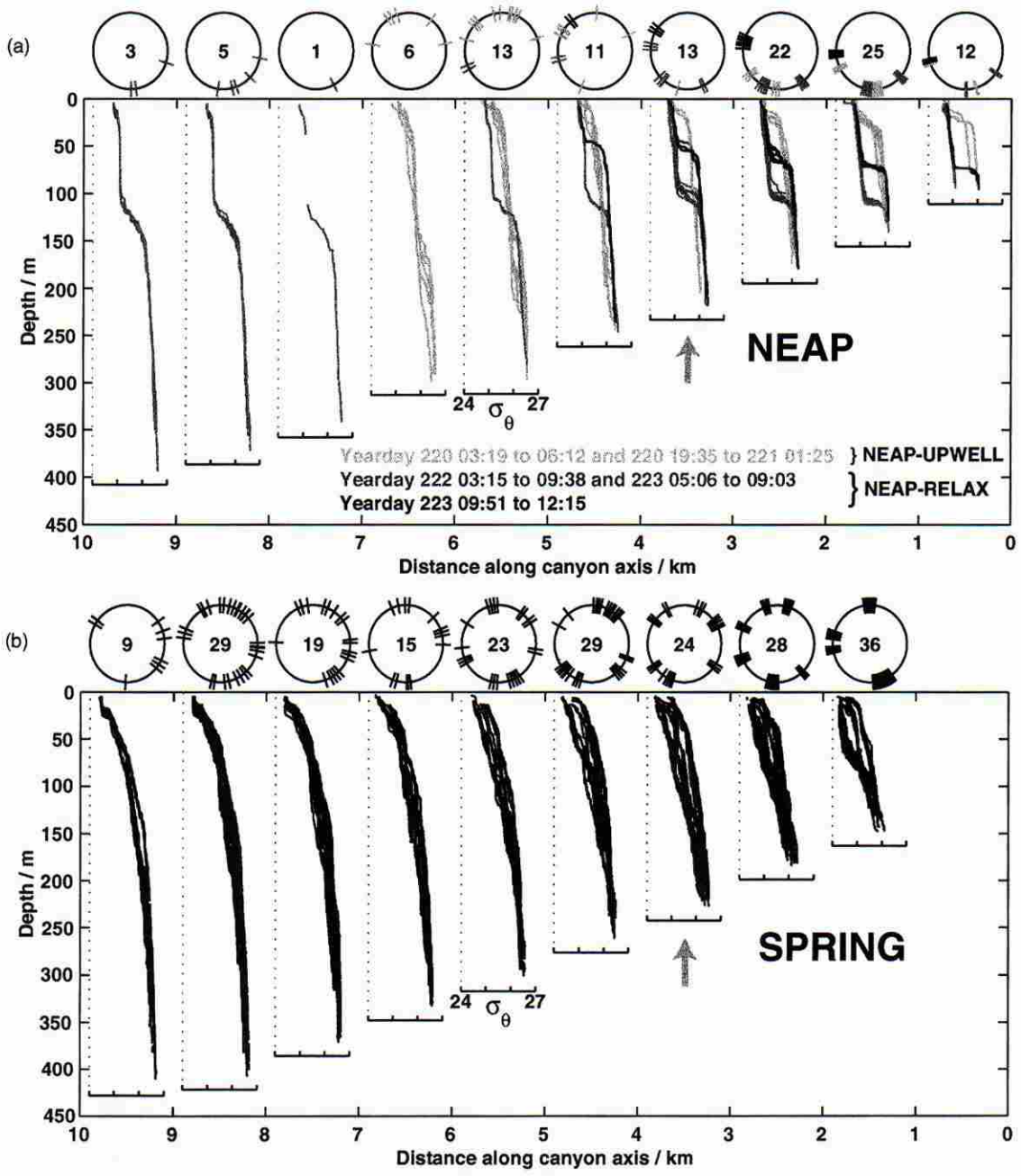

FIG. 3. Density profiles grouped into 1-km along-axis bins: (a) drops during neap tide and (b) during spring tide. The two locations of the pycnocline during the neap-relax state are plotted separately (section 2c). The tidal phase of the drops is indicated by the location on the circles, the left hemisphere representing flood and the right hemisphere ebb. The numbers in the circles give the number of drops plotted for each bin. Arrows mark the 1-km bin between 3 and 4 km used in Fig. 4.

At approximately 200 mab in the height-averaged ε profile, a threefold decrease in magnitude and change in slope may indicate a change in processes between the lower and upper water column.

b. Mixing higher during spring than neap tide

Averaging the data within 10 km of Moss Landing into 500-m along-axis bins (Fig. 6) showed large differences in dissipation, diapycnal diffusivity, stratification, shear-squared, and inverse Richardson number between neap (yeardays 220–223) and spring tide (yeardays 229–233). The high dissipation (Figs. 6a,b) and diapycnal diffusivity (Figs. 6c,d) occurred mainly in stratified water in the lower water column. The thickness of this elevated turbulence layer varied from 70 to 100 m during neap to ~200 m during spring tide. Although it defies a precise definition, it is convenient to denote

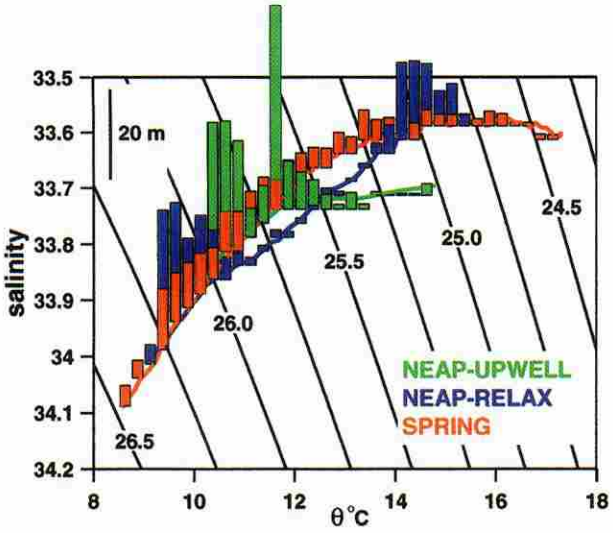

FIG. 4. Average volumetric θ, s curves for drops between 3 and 4 km from the canyon head. The height of the column gives the amount of the water column (in meters) that fell within a given θ, s bin. Three curves have been plotted representing the different density structures observed (Fig. 3), the two different locations of the sharp neap pycnocline have been combined as they have the same θ, s curve.

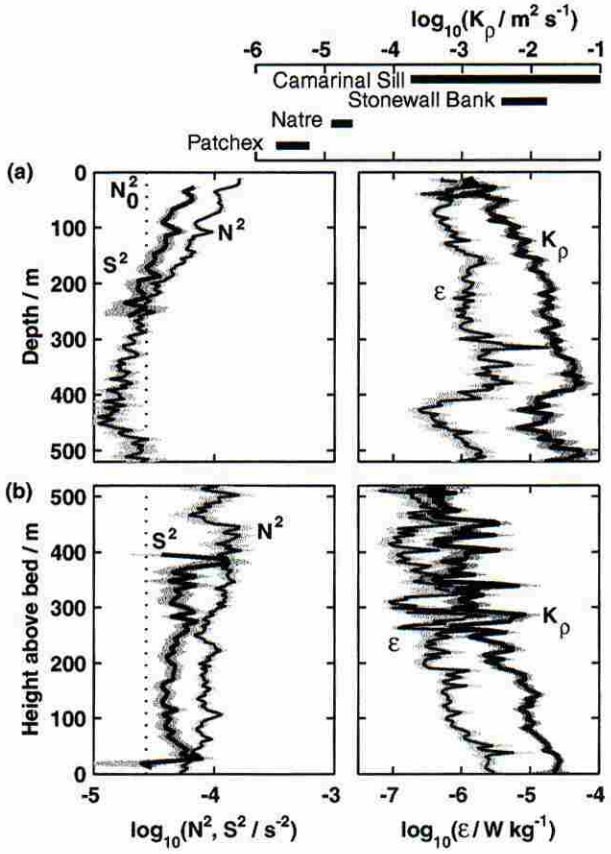

FIG. 5. Average profiles of ε, K_ρ, S^2, and N^2 for microstructure drops taken in Monterey Canyon within 15 km of Moss Landing. These drops were mainly along the canyon axis but included a cross-canyon survey (Fig. 2a): (a) depth-averaged and (b) height-above-bed-averaged profiles. The gray shading gives the 95% bootstrapped confidence interval for the mean. Here $N_0 = 0.0052\ s^{-1}$ is the assumed background stratification level in the Garrett–Munk internal wave spectra. The K_ρ axis has been extended to compare Monterey Canyon with other locations: Carminal Sill, Gibraltar (Wesson and Gregg 1994); Stonewall Bank, OR (Nash and Moum 2001); North Atlantic Tracer Release Experiment (NATRE; Ledwell et al. 1993); and the California Current (PATCHEX; Gregg and Sanford 1988).

this lower section of the water column with elevated mixing as a stratified turbulent layer (STL). There is no reason to suggest that this stratified turbulent layer is associated with local boundary friction processes. In fact, near the open ocean ε and K_ρ values were observed within 20 m of the bed, below the STL, during neap tide (between 3 and 5 km, Fig. 6) and the thickness of the STL argues against local boundary processes. Observed mixing intensity was variable both within and between the 500-m spatially averaged bins. The variation between bins was more pronounced during neap tide.

The average currents corresponding to spring and neap observations were 0.13 and 0.09 m s^{-1}, respectively, which were significantly larger than the $O(0.01$ m $s^{-1})$ barotropic velocities inferred by Petruncio et al. (1998). Maximum current speeds we observed were in excess of 0.4 m s^{-1}. Over the same period, a bottom-mounted ADCP recorded near-bottom velocities up to 0.6 m s^{-1} associated with tidal bores (Key 1999).

During spring tide, dissipation values reached $>10^{-4}$ W kg^{-1} with $\overline{\varepsilon} = 1.8 \times 10^{-6}$ W kg^{-1} (95% confidence interval of $[1.5 \times 10^{-6}$–$2.2 \times 10^{-6}]$ W kg^{-1}) and diapycnal diffusivity reached 8×10^{-2} m^2 s^{-1} with $\overline{K_\rho} = 1.3 \times 10^{-2}$ m^2 s^{-1}($[1.1 \times 10^{-2}$–$1.6 \times 10^{-2}]$ m^2 s^{-1}). The turbulence was mainly in the STL, which had a thickness of ≈200 m with $\langle\varepsilon\rangle = 2.3 \times 10^{-6}$ W kg^{-1} and $\langle K_\rho\rangle = 1.9 \times 10^{-2}$ m^2 s^{-1}. Here angle brackets denote an average over the STL (200 mab for spring, 100 mab for neap tide), whereas overbars denote an average over the water column. Below the ~40-m-thick surface layer but above the STL, K_ρ approached open ocean levels. Figure 7l shows an obvious turbulent layer; there was an increase of 100 times in ε from 150 and 170 m, although, in many other drops, the STL was not sharply defined (e.g., Figs. 7d,h).

During neap tide, $\overline{\varepsilon} = 2.5 \times 10^{-7}$ W kg^{-1}($[2.1 \times 10^{-7}$–$3.0 \times 10^{-7}]$ W kg^{-1}) with a maximum value of 10^{-6} W kg^{-1}, and $\overline{K_\rho} = 2.6 \times 10^{-3}$ m^2 s^{-1}($[2.1 \times 10^{-3}$–$3.1 \times 10^{-3}]$ m^2 s^{-1}) with a maximum $>10^{-2}$ m^2 s^{-1}. Here the STL was 70–100 m thick with $\langle\varepsilon\rangle = 3.9 \times 10^{-7}$ W kg^{-1} and $\langle K_\rho\rangle = 4.3 \times 10^{-3}$ m^2 s^{-1}. Between 8 and 10 km increased turbulence was observed throughout the water column. Nearer the head, the upper-water-column dissipation and diffusivity values approached open ocean levels. A strong STL delimitation was not obvious in some drops (e.g., Figs. 8d,l) but was more pronounced in others (e.g., Fig. 8h).

Spring tide shears (Fig. 6e) were calculated by first differencing the 8-m narrowband ADCP velocities, while neap (Fig. 6f) had to be preprocessed to get equivalent 8-m velocities from the 4-m broadband ADCP.[3] Some caution should be used in comparing spring and neap shears because of differences in signal encoding and variance levels between narrowband and broadband instruments (RDI 1996). The shear range and mean values were similar between spring and neap, with areas of increased shear tending to overlay the strongest stratification. Little correspondence between 8-m shear and elevated turbulence was observed, although the ADCP did not penetrate deep enough to survey the STL.

During spring tide (Fig. 6g) the maximum stratification ($N^2 \approx 10^{-3}$ s^{-1}) occurred near the surface (15–40 m) and decreases with depth to $N^2 \approx 10^{-6}$ s^{-2}. There was some horizontal structure, with bands 10–20 m thick extending for several kilometers. Near the head, the depth of the pycnocline deepens to almost 70 m owing to increased mixing at a shear interface 50–70 m deep.

During neap tide, three high stratification layers (0, 70, and 115 m; Fig. 6h) near the head represent the position of the pycnocline at different times (section 2c). The single deep pycnocline observed between 8 and 10 km was from a single burst and may be time varying like those closer to the head. Profiles of N^2 (Fig. 8) generally showed low stratification above a pronounced pycnocline.

There was no obvious correspondence between elevated turbulence and 8-m inverse Richardson numbers[4] (Figs. 6i,j). For example, one of the largest critical patches ($\mathrm{Ri}^{-1} > 4$) was during neap tide in low stratification between 8 and 10 km, which had low dissipation ($\varepsilon \approx 10^{-8}$ W kg^{-1}). This lack of correspondence between Ri^{-1} and ε is explored further in section 6b.

c. *Mixing locations change from ebb to flood*

Both dissipation (Figs. 9a,b) and diapycnal diffusivity (Figs. 9c,d) suggest that the turbulent regions lay more toward the canyon head during ebb tide than flood. The largest regions of $\varepsilon > 10^{-5}$ W kg^{-1} occurred at 2–8 km during ebb and 6–10 km during flood. Least squares regression on average ε values within each 500-m bin confirmed this trend. The ebb-average dissipation increased toward the head with a slope of 0.093 W kg^{-1} km^{-1} (the 95% confidence interval on the slope was [0.022–0.164]), and the flood-average decreased at a rate of -0.053 W kg^{-1} km^{-1} (95% confidence interval of [-0.085 to -0.022]). During ebb tide high ε and K_ρ were confined to within approximately 170 m of the bed. During flood the high turbulence regions were more intermittent and spread higher into the water column. Turbulent values were generally smaller at 12–15 km than nearer the head.

During the flood phase of spring tide, average dissipation was $\overline{\varepsilon} = 1.2 \times 10^{-6}$ W kg^{-1} (95% confidence interval of [1.0×10^{-6}–1.4×10^{-6}] W kg^{-1}) and $\overline{K_\rho} = 1.6 \times 10^{-2}$ m^2 s^{-1} ([1.3×10^{-2}–1.9×10^{-2}] m^2 s^{-1}). During ebb, $\overline{\varepsilon} = 1.5 \times 10^{-6}$ W kg^{-1} ([1.2×10^{-6}–1.9×10^{-6}] W kg^{-1}) and $\overline{K_\rho} = 1.3 \times 10^{-2}$ m^2 s^{-1} ([1.1×10^{-2}–1.7×10^{-2}] m^2 s^{-1}). So, although there were differences in the location of turbulent dissipation between flood and ebb, the observed magnitude can be considered constant, with $\overline{\varepsilon}$ and $\overline{K_\rho}$ being within a factor of 2 (Osborn 1980; Oakey 1982).

During both flood and ebb, regions of high ε and K_ρ corresponded to an M_4 characteristic (Fig. 9, white lines). Frequency spectra in Kunze et al. (2002) show a definite M_4 peak, which was weaker than the dominant M_2 and intensified toward the bed. The M_4 characteristic appeared confined to the fairly straight canyon axis section between a sweeping meander at 7.5 km and a sharp bend at 4 km implying that, if these were characteristics, the generation may have been from the sidewalls within the canyon meander.

Contours of 8-m shear are shown in Figs. 9e and 9f; unfortunately the survey between 12 and 15 km was conducted in the period when no ADCP data were available. Both shear and stratification (Figs. 9g,h) showed the same pattern as the spring data (section 3b); that is, the largest values were near the surface decreasing with depth.

Within 3 km of Moss Landing during ebb tide, there was a strong baroclinic shear layer at depth 50 m that corresponded to elevated dissipation and 8-m Ri^{-1} between 1.2 and 2. Initially the velocity structure was two layered (NE flow above and WSW below 50 m). Once the velocity structured homogenized, the shear, Ri^{-1}, and dissipation signal disappeared. During flood tide, a series of elevated Ri^{-1} lay along a diagonal which corresponded well with elevated ε and K_ρ and had the slope of a M_4 characteristic (Fig. 9, white lines). Apart from these two examples, the turbulence was not correlated to finescale (8 m) shear and stratification.

d. *Mixing strongest on canyon axis*

A 22-h repeated cross-canyon survey, conducted 9.1 km from Moss Landing between yearday 226 1457 and 227 1225, agreed with along-canyon observations in that most of the turbulence (Figs. 10a–d) was in a lower-water-column stratified turbulent layer. However, it also illustrated that the turbulence tended to be concentrated at the canyon axis. Unfortunately, the broadband ADCP

[3] ADCPs calculate the bin averaged velocity using 50% overlapping Bartlett (triangular) filters of twice the bin length. Combining three overlapping 8-m Bartlett filters (4-m ADCP) with weightings of 0.25, 0.5, and 0.25 is equivalent to one 16-m Bartlett filter (8-m ADCP). Shears were then calculated by taking first differences of these equivalent 8-m velocities.

[4] In order to best represent the stratification being acted on by the shear field, 8-m shears and stratifications were averaged across all the drops in each 500-m bin before taking the ratio.

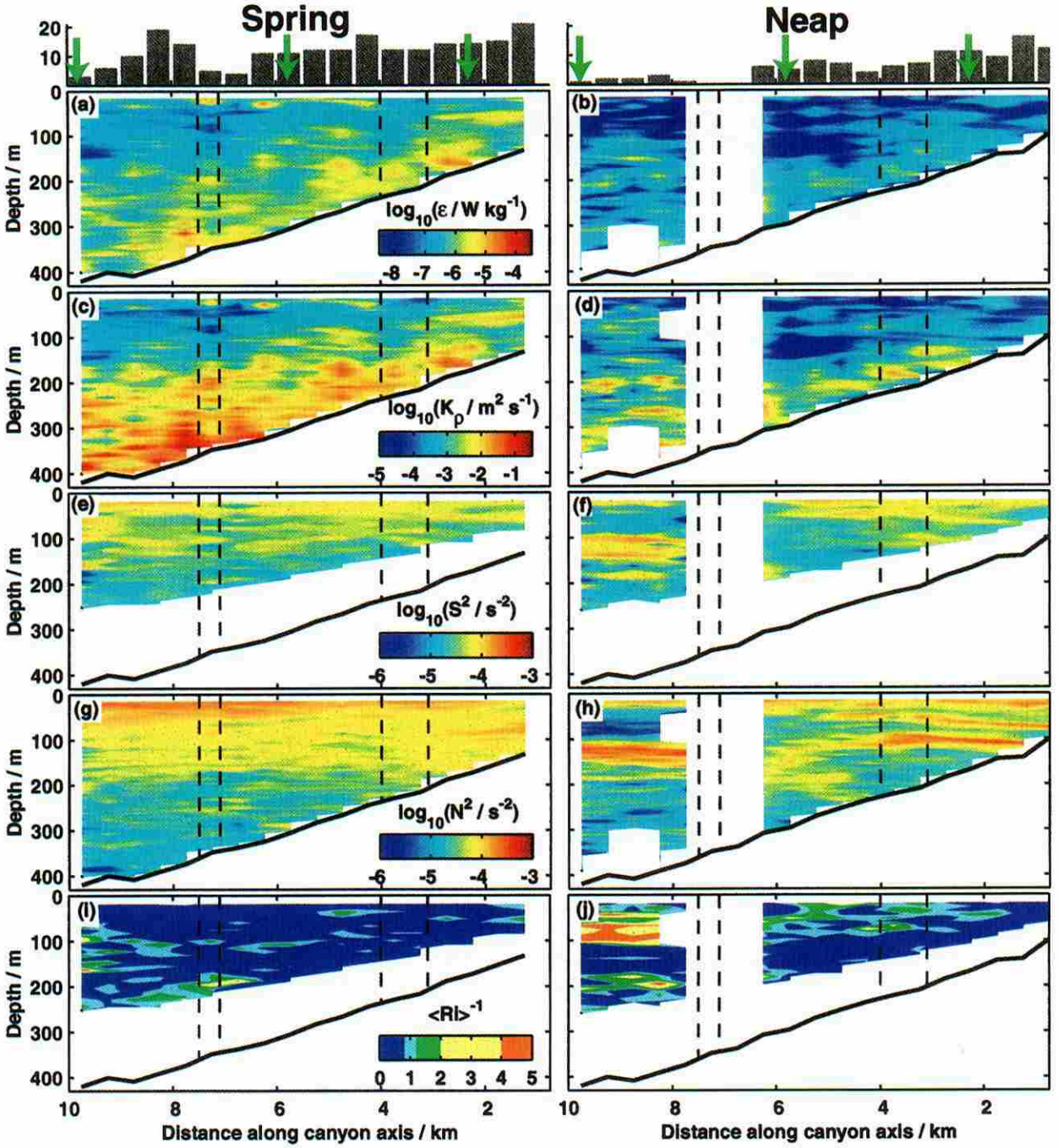

FIG. 6. Contour plots of along-canyon bin-averaged ε, K_ρ, S^2, N^2, and Ri^{-1}. The left column shows spring tide and the right column shows neap. The solid black line is bottom depth measured by the pressure sensor and altimeter on the instrument. The histograms show the number of drops that went into each 500-m average; only drops within 250 m of the canyon axis were included. The green arrows show the location of sample profiles plotted in Figs. 7 and 8 and the dashed vertical lines mark the location of major meanders (3.1, 4.0, 7.1–7.5 km) in the canyon axis.

power supply failed approximately halfway through this survey. Contours of shear and Ri^{-1} are based on averages prior to the failure.

The average velocity structure (not shown) had southeastward flow in the upper 50 m during both flood and ebb. This flow became stronger and less homogeneous over the northern rim. During flood tide, there was a northward flow confined between 50 and 130 m over the southern wall, which had magnitudes up to 0.3 m s^{-1}. This widened and weakened with distance northward across the canyon. During ebb tide, a weak northward flow layer was observed between 50 and 100 m

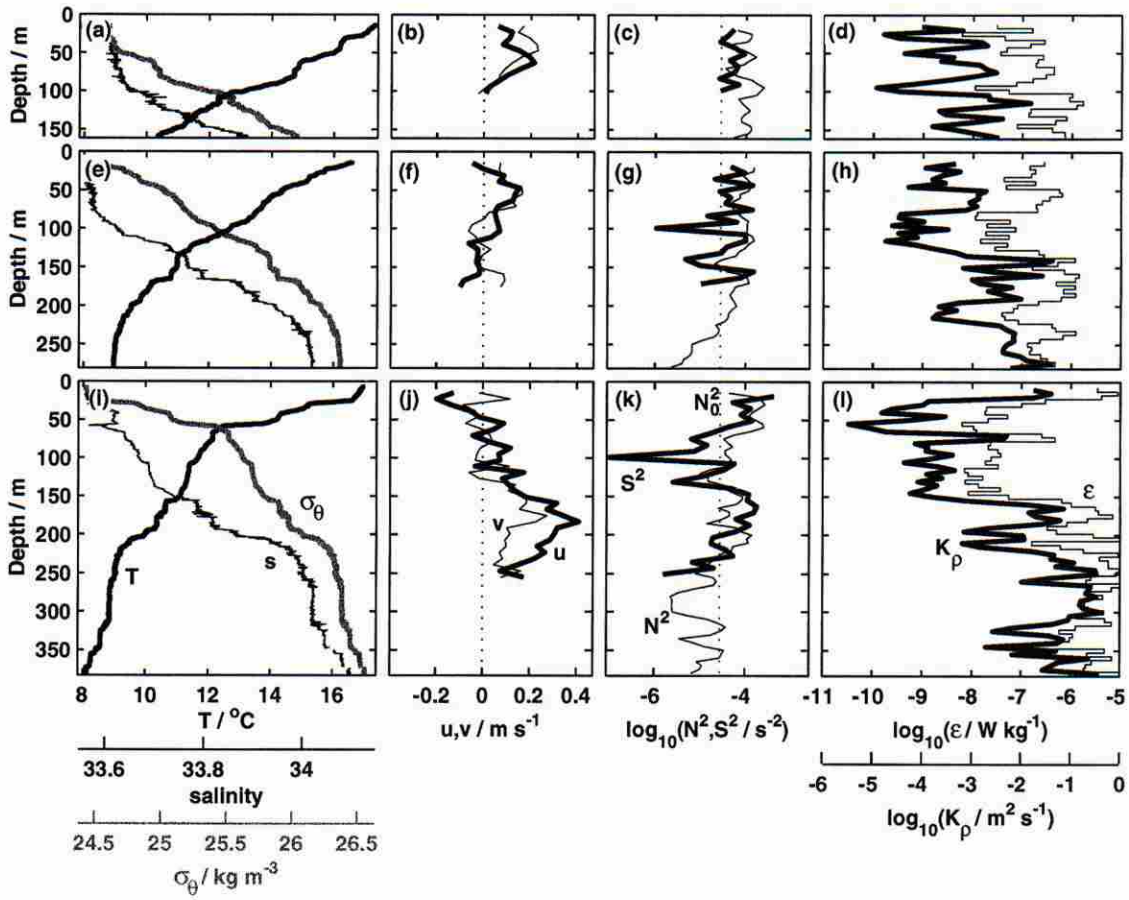

FIG. 7. Spring tide examples of individual profiles of temperature, salinity, potential density, velocity, 8-m shear-squared, stratification, dissipation, and diapycnal diffusivity. The velocities are aligned so that v is positive toward true north. The displayed drops are (a)–(d) AMP16853, 2.44 km from Moss Landing with a bottom depth of 166 m; (e)–(h) AMP16940, 5.64 km, 287 m deep; and (i)–(l) AMP16753, 9.52 km, 390 m deep. The corresponding bin locations are marked in Fig. 6 with a green arrow.

across the canyon; the remainder of the water column contained mainly southwestward flow.

At the canyon axis, the STL was about 130 m thick. This survey, which took place early in the spring tide, had an on-axis STL thickness between those observed during neap and spring tide (section 3b). Off axis, the stratified turbulent layer thickness was approximately 50 m. The exception was near the southern shelf break (0.75 km) during flood tide, which was associated with observed strong northward flow. Visually there seemed to be more turbulence on the north wall during ebb than flood; however, no significant trend was found.

During flood, the average observed cross-canyon dissipation was 1.1×10^{-6} W kg^{-1} (95% confidence interval of $[0.7 \times 10^{-6}$–$1.6 \times 10^{-6}]$ W kg^{-1}) with $\overline{K_\rho} = 1.3 \times 10^{-2}$ m^2 s^{-1} ($[0.7 \times 10^{-2}$–$2.1 \times 10^{-2}]$ m^2 s^{-1}). During ebb, $\overline{\varepsilon} = 1.0 \times 10^{-6}$ W kg^{-1} ($[0.8 \times 10^{-6}$–$1.4 \times 10^{-6}]$ W kg^{-1}) and $\overline{K_\rho} = 9.5 \times 10^{-3}$ m^2 s^{-1} ($[0.5 \times 10^{-2}$–$1.4 \times 10^{-2}]$ m^2 s^{-1}). In agreement with the along-canyon observations (section 3c), the average flood and ebb turbulence values are within a factor of 2, indicating no significant difference.

Observed 8-m shear (Figs. 10e,f) was highest along the surface flow layer interface during both flood and ebb tides. During flood, elevated shear was also observed between 100 and 130 m above the southern wall, which corresponded to the strong northward flow region. Stratification (Figs. 10g,h) followed the same pattern as the spring data (section 3b).

Contours of 8-m Ri^{-1} are shown in Figs. 10i and 10j. There was a critical region (Ri$^{-1} > 4$) associated with the strong northward current along the southern wall during flood. Most of the shear layer at the base of the surface flow has Ri$^{-1} > 1$ during both flood and ebb. Throughout the center of the canyon there were regions of elevated Ri^{-1} that correspond to neither high shear nor high dissipation.

e. *Influence of topography and stratification*

When internal waves reflect off solid boundaries some energy must be dissipated and, if the surface is rough, scattering also occurs (Thorpe 2001). Therefore, when a propagating internal wave encounters a significant

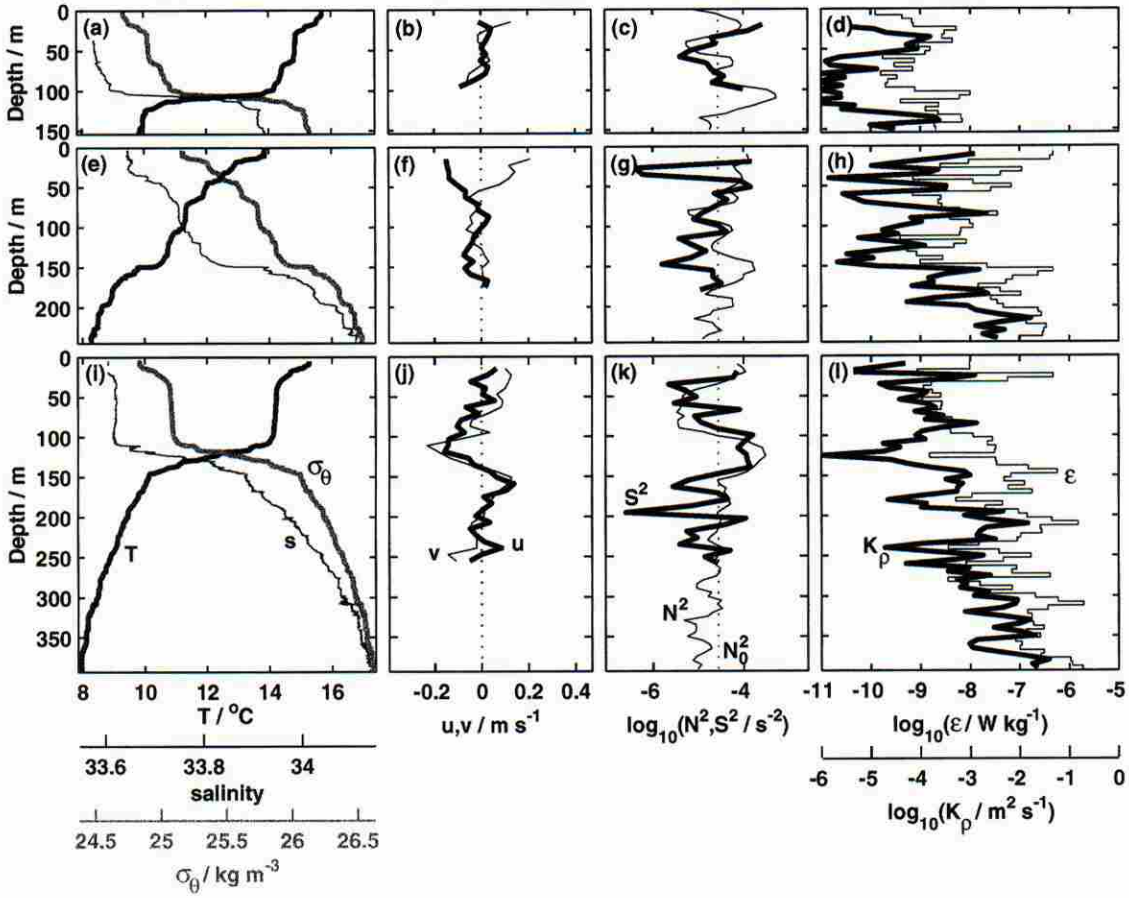

FIG. 8. Neap tide examples of individual profiles of temperature, salinity, potential density, velocity, 8-m shear-squared, stratification, dissipation, and diapycnal diffusivity. The velocities are aligned so that v is positive toward true north. The displayed drops are (a)–(d) MMP6484, 2.30 km from Moss Landing with a bottom depth of 159 m; (e)–(h) MMP6445, 5.58 km, 249 m deep; and (i)–(l) AMP16284, 9.73 km, 398 m deep. The corresponding bin locations are marked in Fig. 6 with a green arrow. [The altimeter was not working during AMP16284, so the bottom depth was estimated by maximum depth surveyed plus the median height above the bed profiles were terminated (5.3 m)].

canyon axis bend, we might expect increased dissipation and possibly a shadow zone (low dissipation due to reduced internal wave activity) behind the bend.

Monterey Canyon axis follows a tortuous path, including some large bends and contributing canyons (Fig. 1). Within 10 km of Moss Landing, where our study was focused, there are major bends at 3.1 and 4.0 km, and a sweeping one between 7.1 and 7.5 km. These bends are marked with vertical dashed lines in Figs. 6 and 9. Neither ε nor K_ρ contours showed levels at the bends different from elsewhere in the canyon, suggesting that the mechanisms were more complicated than an externally generated (linear) internal wave propagating up canyon.

Average dissipation values for each density state were calculated in relatively straight sections between the major bends (Fig. 11a). The three sections, all 2 km long, were between 8 and 10 km, 4.5 and 6.5 km, and 1 and 3 km. For spring and neap-upwell states average dissipations were essentially constant throughout the last 10 km of the canyon. The spring case showed a slight increasing trend toward the head, but the total increase was only 2.5 times. Likewise, there was a slight decreasing trend in the neap-upwell case; this state was not surveyed between 8 and 10 km, so only two points are available. The neap-relax density state, on the other hand, showed marked changes in $\overline{\varepsilon}$ between sections. The average dissipation between 8 and 10 km was 3.5×10^{-7} W kg^{-1}, which decreased by 60-fold to 5.7×10^{-9} W kg^{-1} between 4.5 and 6.5 km (after the sweeping bend) before increasing to 9.2×10^{-8} W kg^{-1} after the bends at 3.1 and 4.0 km.

Normalized distributions of ε data within each 2-km section mainly showed reasonable agreement with a lognormal distribution based on the mean and variance of the $\log_{10}$ transformed data. The neap-upwell and spring distributions have similar along-canyon variances, with the standard deviation varying by less than 20% between the sections. The neap-relax data between 1 and 3 km was visually nonlognormally distributed. Recalculating the distributions separating the neap-relax data based on the two observed pycnocline depths (Fig. 3a) suggested

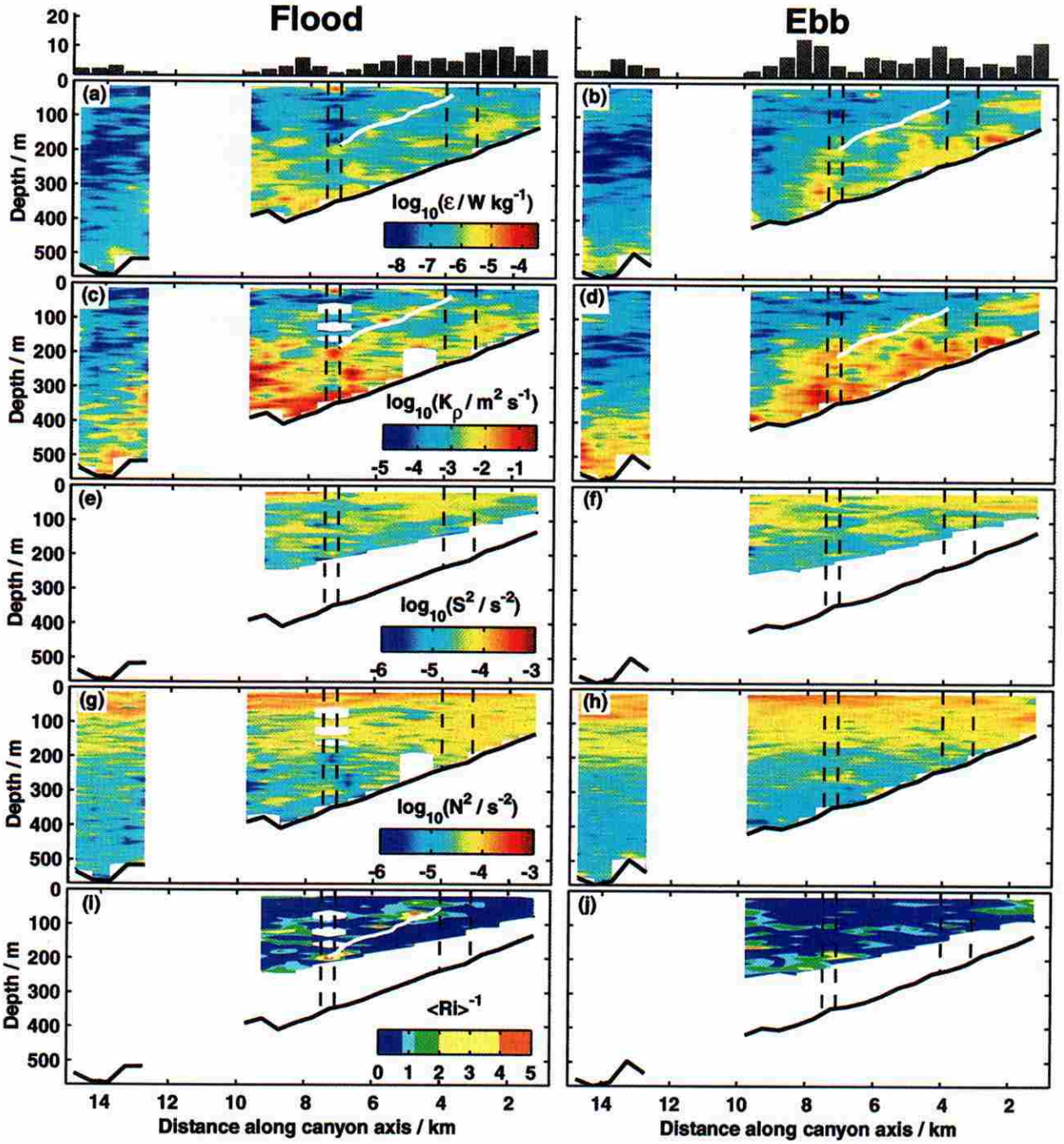

FIG. 9. Contour plots of along-canyon bin-averaged ε, K_ρ, S^2, N^2, and Ri^{-1}. The left column is flood tide (increasing surface elevation) and the right column is ebb (decreasing surface elevation), using data during spring tide. The spring tide data, in addition to having a stronger turbulent signal, were more numerous and better distributed throughout the tidal cycle (Fig. 3). Contouring all the data increased the areas of high S^2 and N^2 without significantly altering ε and K_ρ patterns. The solid black line is bottom depth measured by the pressure sensor and altimeter on the instrument. The histograms show the number of drops that went into each 500-m average. The dashed vertical lines mark the location of major meanders in the canyon axis. The white lines in (a)–(d) and (i) indicate the slope of the M_4 characteristic.

there were two distinct distributions (Fig. 11b). When the pycnocline was in the deeper location (yeardays 222 0315–223 0903), average dissipation decreased from 3.5×10^{-7} W kg^{-1} between 8 and 10 km to 3.9×10^{-9} W kg^{-1} between 4.5 and 6.5 km and remained nearly constant to the between 1 and 3 km section (6.9×10^{-9} W kg^{-1}). When the pycnocline was higher in the water column (yearday 223 0951–1215), there were no ob-

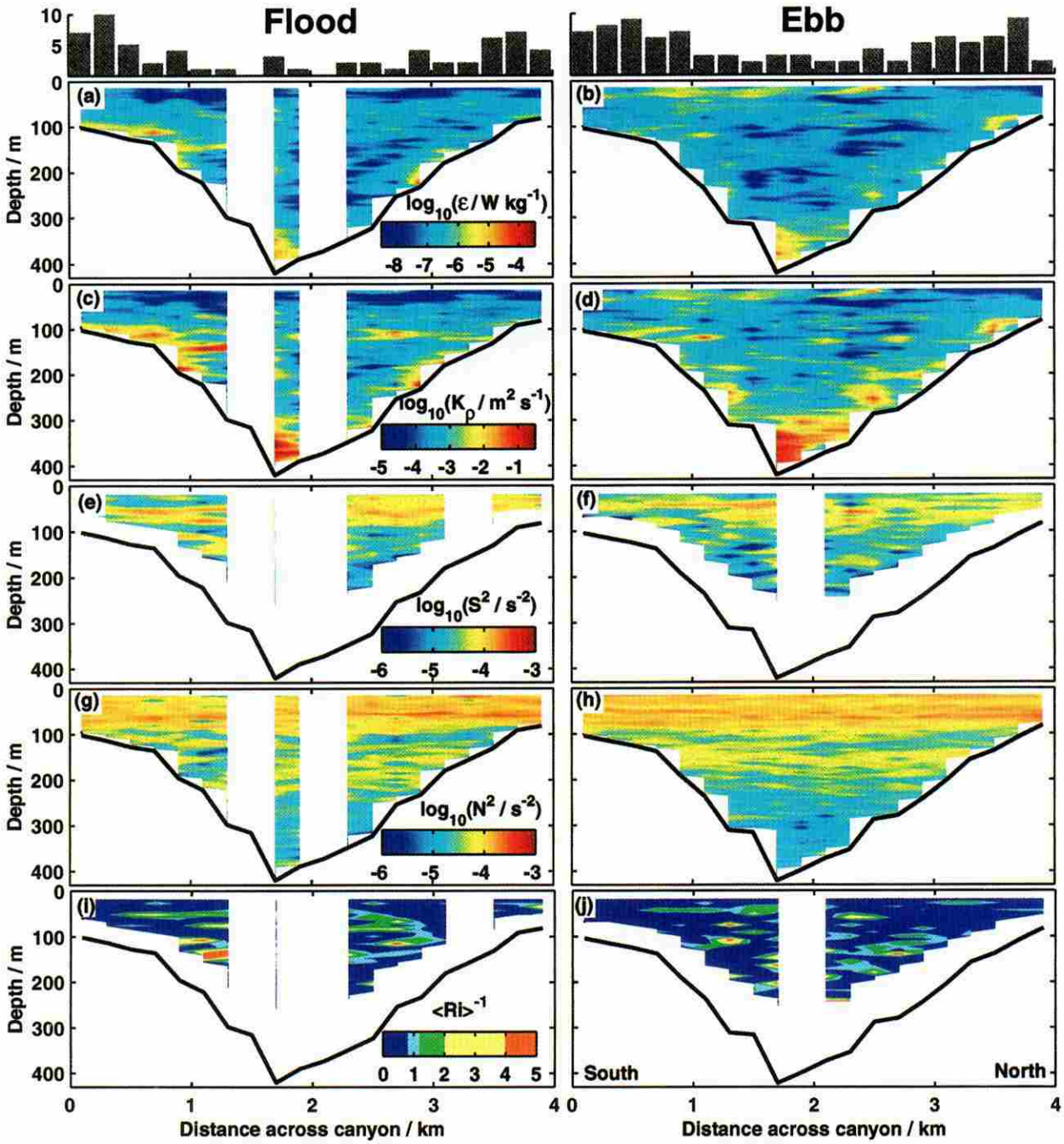

FIG. 10. Contour plots of across-canyon bin-averaged ε, K_ρ, S^2, N^2, and Ri^{-1}. The cross-canyon survey took place over a 22-h period, 9.1 km from the canyon head (Fig. 2a). The left column is flood tide (increasing surface elevation) and the right column is ebb (decreasing surface elevation). The solid black line is the bottom depth measured by the pressure sensor and altimeter on the instrument. The histograms show the number of drops that went into each 200-m average. The ADCP power supply failed during this survey so the shear and Ri^{-1} averages only include half as many drops.

servations between 8 and 10 km, but in the other two sections average dissipation was elevated above what was observed with the deeper pycnocline. Between 4.5 and 6.5 km $\overline{\varepsilon}$ was 1.1×10^{-8} W kg^{-1}, which increased to $\overline{\varepsilon} = 2.4 \times 10^{-7}$ W kg^{-1} between 1 and 3 km. Therefore, within the neap-relax state, the two observed pycnocline depths resulted in an ~35-fold change in average dissipation. Other analysis (not shown) indicated that dissipation levels were often lower above the pycnocline (regardless of pycnocline position), although there was no significant change in the corresponding 8-m shear distributions.

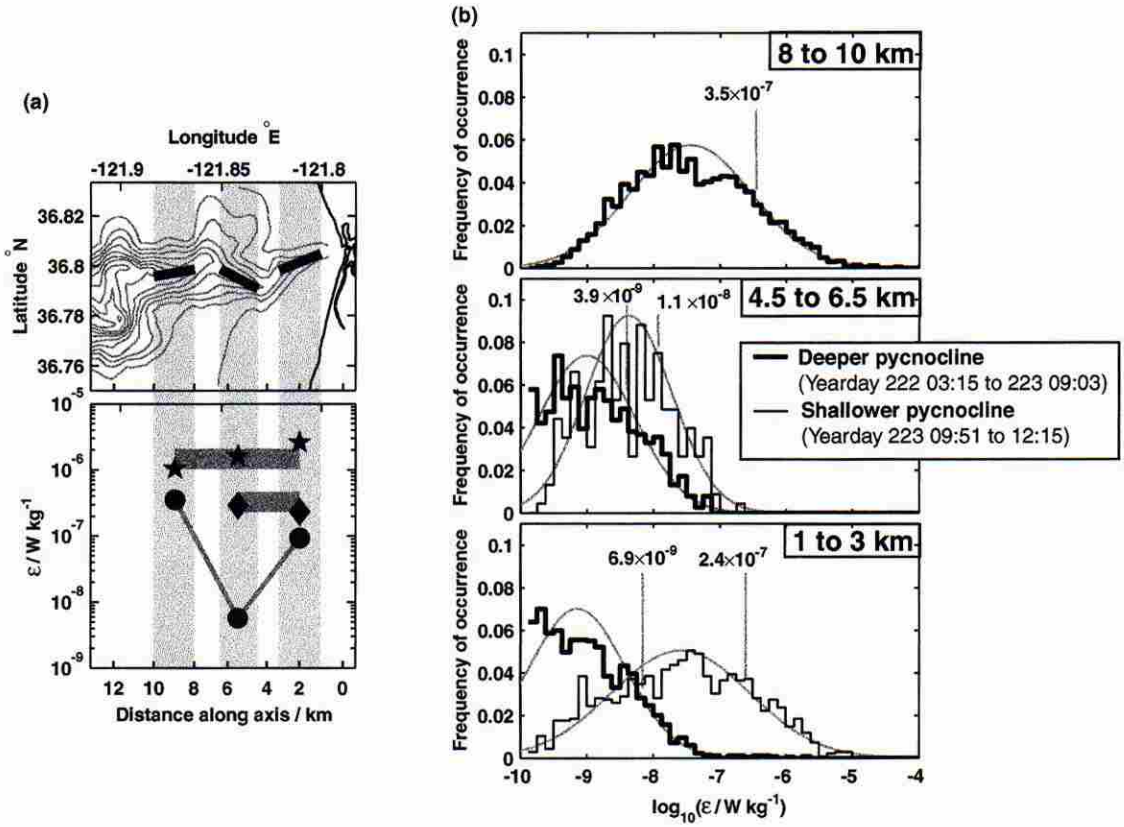

FIG. 11. (a) Average dissipation values in 2-km along-canyon sections where the canyon axis is fairly straight but each section is separated by significant bends. The sections are between 8 and 10 km, 4.5 and 6.5 km, and 1 and 3 km. Averages are plotted for each density state: neap-upwell (diamond), neap-relax (circle), and spring (star). The thick horizontal lines give a factor of 2 on the smallest ε, showing these values are nearly constant. (b) Distributions of dissipation in the 2-km sections for the two observed positions of the pycnocline during the neap-relax density state. Gray curves show the corresponding Gaussian distribution with the same mean and standard deviation as the data. Mean values for each distribution (W kg^{-1}) are also shown.

From our limited temporal survey, it would appear that dissipation during the neap-relax density state was sensitive to canyon axis bends and position of the pycnocline.

f. Comparison to other locations

A key result of this work is that the observed diapycnal diffusivities near the head of Monterey Canyon ($\overline{K_\rho} = 1.0 \times 10^{-2}$ m^2 s^{-1}) were among the highest observed anywhere, including known hotspots such as fronts, warm-core rings, and near topography (Gregg 1998; Gregg et al. 1999), as well as being 10–10^3 times greater than those observed in the open ocean (Gregg 1998). To date, only observations of hydraulically controlled flows yield similar diapycnal diffusivities, that is, upper-ocean hotspots: $\overline{K_\rho} = 550 \times 10^{-4}$ m^2 s^{-1} over Carmarinal Sill, Gibraltar (Wesson and Gregg 1994; Gregg 1998); $\overline{K_\rho} = 37 - 170 \times 10^{-4}$ m^2 s^{-1} over Stonewall Bank, Oregon (Nash and Moum 2001); and inferences at abyssal constrictions: $\overline{K_\rho} = 1000 \times 10^{-4}$ m^2 s^{-1} through the Romanche Fracture Zone (Ferron et al. 1998) and $K_\rho = 5 \times 10^{-2}$ m^2 s^{-1} in the abyssal flow through Samoan Passage (Roemmich et al. 1996).

The high diapycnal diffusivity values in Monterey Canyon are not simply the result of well mixed water [low N^2 in Eq. (2)]. The stratification we observed ($\overline{N^2} = 6.8 \times 10^{-5}$ s^{-2}) was stronger than the $N^2 = 1$–4×10^{-6} s^{-2} associated with enhanced mixing above the abyssal ocean floor (Moum et al. 2002).

The observed turbulent kinetic energy dissipation rates ($\overline{\varepsilon} = 1.1 \times 10^{-6}$ W kg^{-1}) were similar to Stonewall Bank (Nash and Moum 2001), Knight Inlet (J. Klymak and M. Gregg 2002, manuscript submitted to *J. Phys. Oceanogr.*), and slightly higher than the Romanche Fracture Zone where $\varepsilon \lesssim 1 \times 10^{-6}$ W kg^{-1} (Polzin et al. 1996). However, Monterey Canyon was up to three orders of magnitude lower than Carmarinal Sill, where average dissipations reached 1.8×10^{-3} W kg^{-1} (Wesson and Gregg 1994).

4. Analysis

a. Energy: Fluxes and balance

Spring tide on-axis vertically integrated energy fluxes tended to be up canyon. Within 10 km of the head,

magnitudes were between 0.3 and 1.9 kW m^{-1}, consistent with previous estimates (Petruncio et al. 1998; Kunze et al. 2002), but were smaller than observed close to the mouth during the same period. Both flux convergences and divergences were observed. The magnitude of the flux convergences were comparable to the observed dissipation rates. In the flux divergence regions, local production increased the energy flux up canyon in the presence of strong dissipation.

1) ENERGY FLUXES

The energy flux for an internal wave is

$$\mathbf{F}_E = \overline{p'\mathbf{u}'}, \quad (3)$$

where p' and $\mathbf{u}'$ are pressure and velocity perturbations, and the overbar denotes the mean over a wavelength (Gill 1982). Following Kunze et al. (2002), horizontal energy fluxes were calculated from vertically demeaned velocity and pressure profiles. The pressure perturbation profiles were

$$p'(z) = -g\int_z^0 \rho'\,dz + \frac{g}{H}\int_H^0\int_z^0 \rho'\,dz\,d\zeta, \quad (4)$$

where ρ' was the density anomaly around the mean background state, g is gravitational acceleration, H is water depth, and ζ is a dummy variable of integration.

Energy fluxes were calculated on 1-km along-axis spatial bins (maximum width 500 m). Figure 3, which includes the tidal phase of the microstructure drops, shows that only during spring tide were the drops reasonably well distributed throughout the tidal cycle. Within each spatial bin the drops may have come from more than one tidal cycle. For the two neap density states there was not enough tidal representation to allow reliable flux estimates.

Figure 12a shows that vertically integrated energy fluxes were aligned with local axis direction. All the fluxes are up canyon except the one at 9.5 km. The flux magnitude decreased from 1.5 kW m^{-1} at 8.5 km to 0.3 kW m^{-1} at 6.5 km (after the sweeping bend), then increased to a local maximum of 1.9 kW m^{-1} at 4.5 km; by 1.5 km the flux magnitude decayed to 0.7 kW m^{-1}. Kunze et al. (2002) calculated energy fluxes for the same period between the mouth of the bay and 12 km. They found vertically integrated fluxes of about 5 kW m^{-1} at the mouth decaying nonmonotonically to ~1 kW m^{-1}. Consistent with our observations, only some bends had an associated decrease in up-canyon flux. The downcanyon flux at 9.5 km was positioned on the same ~90° bend as the sole downcanyon flux observed by Kunze et al. (2002). Although it seems this bend differs from the rest of the canyon, it was not surveyed by either experiment. Variability in the fluxes, as well as the presence of downcanyon fluxes, suggests local internal wave generation throughout the canyon.

The largest uncertainties in the energy fluxes came from the difficulties in estimating full-depth background

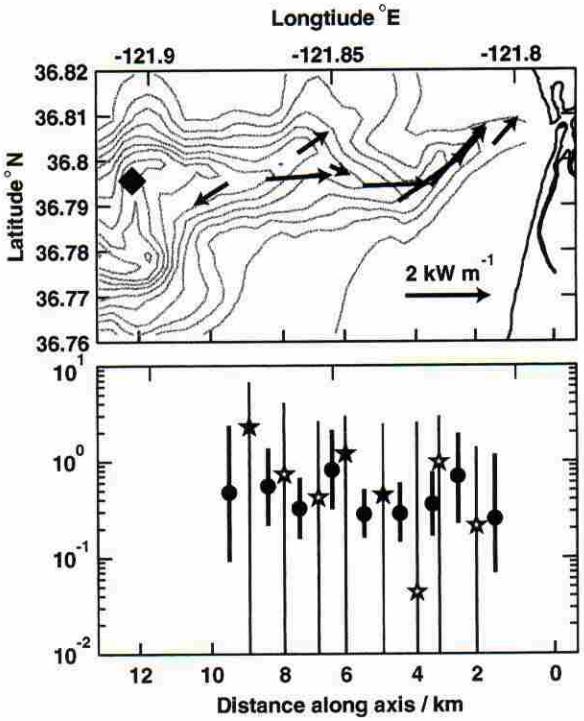

FIG. 12. (a) Vertically integrated energy fluxes in 1-km along-canyon bins for spring tide. The diamond marks the approximate location of the only downcanyon flux observed by Kunze et al. (2002). (b) Comparison of vertically integrated flux convergences and divergences to turbulence production rate. Open stars are flux convergences (energy lost from the internal tide), solid stars are flux divergences, and solid circles are vertically integrated turbulence production rate. Vertical lines give one-standard-deviation error estimates.

profiles. All drops with density gaps greater than 20 m, including at the surface and bed, were discarded. This resulted in the removal of between 1 and 13 drops from each bin. An ADCP cannot make valid velocity measurements near the bed (RDI 1996) and the percentage of water column discarded increases with steep topography (section 6b). Gaps of less than 20 m were linearly interpolated, the first and last values were propagated to the boundaries. Elevated velocities below the valid ADCP depth were expected from the elevated dissipation (Figs. 6a,c) and were observed by Key (1999). Missing these higher velocities may not be important in calculating semidiurnal internal tide fluxes as the highest velocities observed by Key (1999) were associated with tidal bores and Kunze et al. (2002) showed increased contributions from higher harmonics near the bed. Although it is not possible to estimate uncertainty from our data, the flux magnitudes and directions appear to be consistent with Kunze et al. (2002) and Petruncio et al. (1998).

2) ENERGY BALANCE

Petruncio et al. (1998) infer dissipation of $\varepsilon = 1.6$–2.2×10^{-6} W kg^{-1} from the difference in energy flux

between two CTD stations, which is in remarkable agreement with our average observed dissipation ($\overline{\varepsilon} = 1.2 \times 10^{-6}$ W kg^{-1}; section 3a). This is consistent with nearly all the energy of the along-canyon internal tide being lost as turbulence. Kunze et al. (2002) found that flux convergences in the outer canyon were comparable to the microstructure dissipation near the head of the canyon.

The vertically integrated along-canyon balance between energy flux and dissipation is obtained by assuming steady state and neglecting advection, local shear production, and energy lost or gained from off axis (Kunze et al. 2002). The balance is

$$\int_H^0 \frac{\Delta \mathbf{F}_E}{\Delta r}\, dz = \rho_0(1 + \Gamma) \int_H^0 \varepsilon\, dz \quad [\text{W m}^{-2}], \quad (5)$$

where $\Delta \mathbf{F}_E = \Delta(\overline{p'\mathbf{u}'})$ is the upcanyon difference in energy flux, Δr is the upcanyon separation distance, Γ is the mixing efficiency (0.2), and the right-hand side gives the vertically integrated turbulence production rate (i.e., turbulent energy lost to dissipation plus turbulent energy used to increase buoyancy flux).

Figure 12b compares vertically integrated flux convergences and divergences with vertically integrated turbulence production rate. Flux convergences (open stars) represent energy loss from the internal tide (i.e., a larger upcanyon flux entering the bin than leaving), whereas divergences (solid stars) represent a gain of energy. Flux convergence magnitudes were consistent with the observed dissipation, suggesting that in these regions decay of the upcanyon propagating internal tide may account for the observed (intense) dissipation signal. However, the error estimates $[\sqrt{2}\ \overline{\sigma(\mathbf{F}_E)}/\Delta r]$ are large, so this agreement may be fortuitous. The presence of flux divergences required either local production or off-axis advection of energy. Off-axis flux measurements by Kunze et al. (2002) were weak, suggesting that local production was the major mechanism for increasing on-axis energy flux.

Assuming the weak off-axis dissipations (section 3d) and fluxes (Kunze et al. 2002) are representative, the predominant energy balance in Monterey Bay was along the canyon axis. The on-axis energy balance was complex with strong dissipation possibly balanced by decay of the internal tide in some regions and local production required to increase energy flux in the presence of strong dissipation in other regions.

b. *Internal wave spectra*

Figure 13 shows vertical wavenumber spectra of normalized shear and strain calculated in 1-km along-canyon bins for the spring data. These have been corrected for lost variance with transfer functions for a Bartlett filtering (shear) and first differencing (shear and strain) (Alford and Gregg 2001). The shear spectra were normalized by depth-averaged N^2 and were cut off at 4×10^{-2} cpm to avoid instrument rolloff. A Daniell smoothing window (Percival and Walden 1993) was used to reduce high frequency oscillations in the strain spectra. Garrett–Munk spectra (GM76 as defined by Gregg and Kunze 1991) have been plotted as a reference.

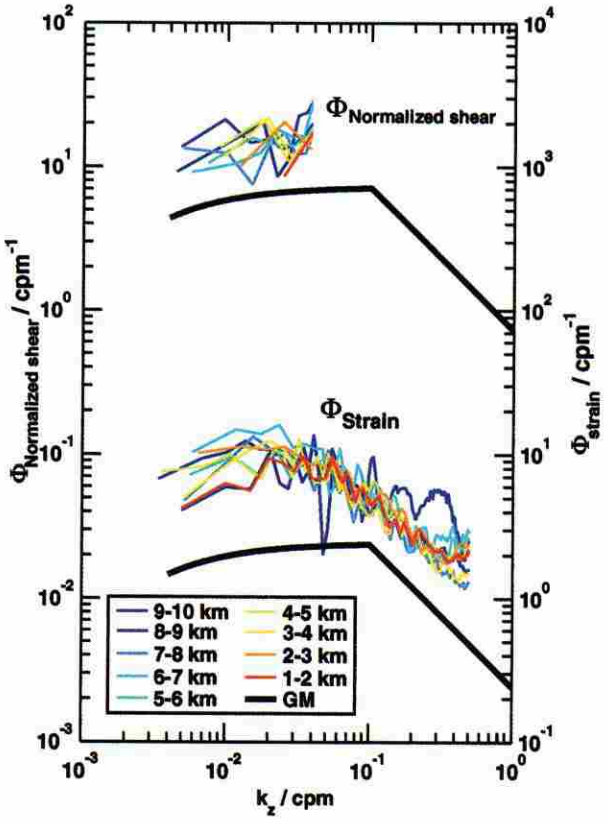

FIG. 13. Vertical wavenumber spectra of shear (normalized by depth-averaged stratification) and strain calculated in 1-km along-canyon bins for the spring data. The Garrett–Munk internal wave spectra are plotted for reference.

Wunsch and Webb (1979) found that velocity spectral levels increased from the continental rise to the mouth of Hydrographer Canyon and into the canyon. No intensification towards the head was visible in our data (i.e., spectral levels from each 1-km bin were similar), possibly because of the much shorter spatial scales involved. However, spectral levels within 10 km of the canyon head were approximately 2 times GM76 for normalized shear and 4 times GM76 for strain. In the outer canyon, Kunze et al. (2002) reported an internal wave field almost an order of magnitude more energetic than that in the open ocean. However, this was close to an upper limit from station averaged kinetic and potential energy profiles so a direct comparison with our spectral levels is not appropriate.

Normalized shear spectra for the two neap states (not shown), which were less reliable because of fewer drops, were similar to those observed during spring. Similar levels (2–4 times GM) have been observed in spectra from below a mesoscale jet during PATCHEX North (Gregg et al. 1996) where ε and K_ρ were 10^3 times lower,

and in the interior of the Straits of Florida (Winkel 1998) where turbulence was $>10^2$ times lower. Gregg et al. (1996) found ε did not appear to be simply related to shear variance and Kunze et al. (2002) noted the rate of transfer from low wavenumbers to high wavenumbers could be important. During COARE leg 3, the rolloff was steeper than the k_z^{-1} of GM76 (Gregg et al. 1996), the dissipation was an order of magnitude lower than PATCHEX North despite having more low wavenumber energy. The steeper slope was suggested to be due to an internal wave field containing only a few dominant waves rather than a continuous distribution in wavenumber and frequency. The strain spectra rolloff from Monterey Canyon (Fig. 13) has a gentler slope than GM76, which we suggest was due to scattering and near-critical reflection off topography pushing energy directly into high wavenumbers. Elevated energy at high wavenumbers required elevated dissipation.

c. *Statistical comparison of ε to S^2, N^2, and Ri^{-1}*

A number of researchers have attempted to relate dissipation to more easily measured finescale shear and stratification. Using data from six midlatitude locations, Gregg (1989) suggested dissipation attributed to internal waves in the open-ocean thermocline could be modeled as $\overline{\varepsilon_{IW}} = 7 \times 10^{-10} \overline{N^2/N_0^2}\ \overline{S_{10}^4/S_{GM}^4}$ W kg^{-1}, where S_{10} is the observed 10-m shear and S_{GM} is the corresponding shear in the Garrett–Munk internal wave spectra. Following the comments of Gargett (1990), Polzin et al. (1995) extended the scaling to account for changes in spectral shape, particularly decreasing cutoff wavenumber with increasing energy level. Kunze et al. (2002) found that the Polzin scaling underestimated dissipation by a factor of 30 in Monterey Canyon.

Figure 14 plots average ε and corresponding 95% bootstrapped confidence interval in logarithmically even bins of 8-m shear, stratification, and Ri^{-1}. Only bins with ≥ 10 data pairs were plotted. For a coastal comparison, data excluding solibores from the 1996 Coastal Mixing and Optics experiment (CMO96) on the New England shelf (MacKinnon and Gregg 2002, manuscript submitted to *J. Phys. Oceanogr.*, hereafter MAG), reprocessed to give equivalent 8-m values,[5] have been plotted.

The spring data has the highest dissipation rates, the two neap states were similar with $\overline{\varepsilon}$ slightly higher during neap upwell. CMO96 dissipation was over 10^2 times lower than our spring data and over an 10 times smaller than the neap data. The 95% confidence intervals tended to reflect the amount of data in each bin.

The ε–S_8^2 comparison (Fig. 14a), which excludes most of the STL (no shear measurements), showed a weak power-law relation. Only neap upwell had a least squares fit that explained more than 50% of the variance ($R^2 = 67\%$). For neap upwell, the best fit was $\varepsilon = 4 \times 10^{-6} |S_8|^{0.56}$ W kg^{-1}. Although this did not explain a high percentage of the variance, the general trend is for dissipation to be proportional to the square root of shear. This implies that dissipation in Monterey Canyon was less sensitive to shear than either on the New England shelf ($\varepsilon \propto |S_4|^{1.2}$; MAG) or in the open ocean thermocline ($\varepsilon \propto |S_{10}|^4$; Gregg 1989; Polzin et al. 1995). This lack of sensitivity may be due to the ADCP not measuring the shear variance sufficiently. However, even if this were a resolution issue, it makes the estimation of dissipation in canyons from ADCP or XCP (Kunze et al. 2002) finescale shears very difficult.

Comparison of ε and N^2 (Fig. 14b) shows dissipation almost independent of stratification for the three density states. While MAG found $\varepsilon(N^2)$ had a nonzero slope for $N^2 > 2 \times 10^{-4}$ s^{-2}, corresponding to elevated shear, the weaker dependence on shear observed in Monterey Canyon would make this effect less pronounced.

The comparison of ε and inverse Richardson number (Fig. 14c), where Ri^{-1} was calculated using 8-m N^2 with no time averaging, showed ε tended to roll off with increasing Ri^{-1}. The spring data, which had a peak between $Ri^{-1} = 2$ and 3 influenced by the two highest shear bins, had very little roll off. In the two neap states dissipation remains nearly constant until $Ri^{-1} \approx 2.5$ when ε levels decreased. The same pattern holds for the CMO96 data except the cutoff was $Ri^{-1} \approx 1.5$. The normalized distributions showed the majority of the data was in the dynamically stable region ($Ri^{-1} < 1$).

Dissipation appeared to be linked to shear by a weak power law ($\varepsilon \propto |S_8|^{0.5}$) but to neither N^2 nor Ri^{-1}. Topography interactions pushing energy directly into high wavenumbers (section 4b) does depart from the wave–wave interactions underlying Gregg (1989) and may account for the observed weaker relation to shear. This analysis was unable to explain why the spring dissipations were higher than those during neap tide. Not only were the shear and stratification ranges the same between the three states but their distributions were also similar. It is possible that had we been able to calculate reliable strain spectra for neap tide, the rolloff may have been closer to k_z^{-1} because of weaker topography interactions.

5. Summary

Microstructure data showed that dissipations and diapycnal diffusivities near the head of Monterey Canyon were among the highest observed anywhere ($\overline{\varepsilon} = 1.1 \times 10^{-6}$ W kg^{-1}; $\overline{K_\rho} = 1.0 \times 10^{-2}$ m^2 s^{-1}). Dissipations were consistent with earlier inferences from energy fluxes in Monterey Canyon (Petruncio et al. 1998).

Turbulence was mainly occurred in stratified water in the lower water column, which we denote as a stratified

[5] The 8-m velocities are calculated from a 4-m ADCP by $0.25v_i + 0.5v_{i+1} + 0.25v_{i+2}$. The 8-m first difference shear from a 4-m ADCP is then given by $[(0.25v_i + 0.5v_{i+1} + 0.25v_{i+2}) - (0.25v_{i+2} + 0.5v_{i+3} + 0.25v_{i+4})]/8$. Equating this with 4-m first difference shears implies weighting of 1/8, 3/8, 3/8, and 1/8 to get 8-m shears from 4-m shears.

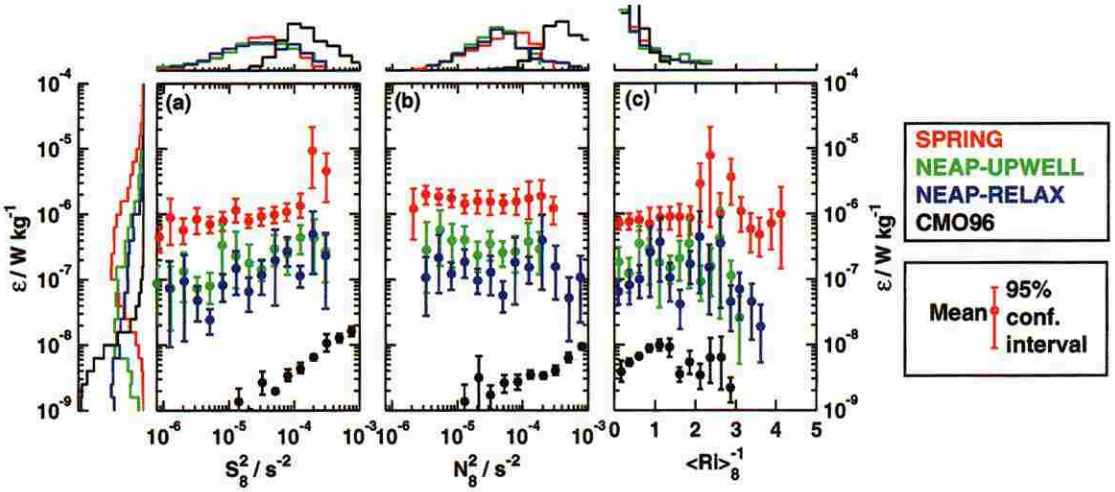

FIG. 14. Dissipation averaged into logarithmically even bins of S^2, N^2, and Ri^{-1}. Along-canyon axis data within 10 km of Moss Landing are separated according to the three density states: neap upwell (green), neap relax (blue), and spring (red). Data from the CMO96 cruise on the New England shelf (MAG) have been reprocessed into 8-m bins and are plotted in black. Average ε and the corresponding 95% confidence interval are plotted for each bin. Normalized distributions of each variable are included. Only bins containing 10 or more dissipation values have been plotted.

turbulent layer (STL). The STL was thickest on the canyon axis and was modulated by the fortnightly tidal cycle. There was an approximately 5 times increase in dissipation ($\langle\varepsilon\rangle_{\text{neap}} = 4.2 \times 10^{-7}$ W kg^{-1} versus $\langle\varepsilon\rangle_{\text{spring}} = 2.3 \times 10^{-6}$ W kg^{-1}) and diapycnal diffusivity ($\langle K_\rho\rangle_{\text{neap}} = 5.1 \times 10^{-3}$ m^2 s^{-1} versus $\langle K_\rho\rangle_{\text{spring}} = 1.8 \times 10^{-2}$ m^2 s^{-1}) averaged over the STL from neap to spring tide. The thickness of the STL was 70–100 m during neap and ~200 m during spring tide. Elevated turbulence lay more toward the canyon head during ebb than flood tide; however, water column averages ($\overline{\varepsilon}$ and $\overline{K_\rho}$) within 10 km of the head could be considered constant between ebb and flood.

Three distinct density states were observed, with advection being the major mechanism altering the density field. During the neap-relax state, which was characterized by the presence of an $O(1$ kg m$^{-3})$ pycnocline, on-axis dissipation levels were sensitive to position relative to axis bends. Dissipation in the other density states (neap-upwell and spring) remained nearly constant throughout the study region. During neap relax, two locations of the pycnocline were observed, the shallower location corresponded to an ~35-fold increase in average dissipation over the deeper location.

On-axis energy fluxes ($\mathbf{F}_E = \overline{p'\mathbf{u}'}$) were aligned with the topography and predominantly up canyon. The flux magnitudes varied nonmonotonically with along-canyon distance, resulting in both flux convergences and divergences. The flux convergences (loss of energy from the internal tide) were consistent with dissipation, although large error estimates suggest this agreement is fortuitous. The presence of flux divergences combined with weak off-axis fluxes suggest local production must be important. Vertical wavenumber spectra were elevated above GM by 2–4 times, a level of elevation similar to that found in locations with 10^2–10^3 times less dissipation. The spring tide strain spectra showed a gentler rolloff than GM suggesting critical reflection and scattering at topography may push energy directly to high wavenumbers. This deviation from wave–wave dynamics (as described by GM) may account for Monterey Canyon's much weaker power-law relation between dissipation and shear ($\varepsilon \propto \sqrt{|S|}$) in comparison with the open ocean ($\varepsilon \propto |S|^4$). Despite similar shear distributions, the spring dissipations were an order of magnitude higher than the two neap states.

6. Discussion

a. *Canyons may be a small but significant fraction of global internal tide mixing budgets*

Estimates of internal tide dissipation range from ~200 GW (Munk 1997) to ~360 GW (Kantha and Tierney 1997). Egbert and Ray (2000) estimate 700 GW for deep-sea M_2 dissipation and, although they do not constrain the mechanisms, they suggest a significant role for internal tides.

We observed a stratified turbulent layer that varied in thickness between $h \approx 70$ and 200 m, and dissipation averaged over the STL between $\langle\varepsilon\rangle = 4.2 \times 10^{-7}$ and 2.3×10^{-6} W kg^{-1}. Assuming these represent the extremes of a sinusoidally varying process, then the time averages are 135 m and 1.36×10^{-6} W kg^{-1}. Hickey (1995) states that canyons can occupy nearly 50% of the shelf edge in some regions and account for 20% of the shelf on the west coast of North America. Estimating the fraction of global shelf occupied by canyons, we assume 10% of the globe's 155 000 km of coastline. Confining our estimate to canyon depths where the can-

yon incises the continental shelf, we somewhat arbitrarily choose 20 km as a representative canyon length, approximately one-third of the global average shelf width (Pickard and Emery 1990). These parameters give a crude estimate for the global dissipation in canyons of 58 GW or 16% of the global internal tide dissipation estimate of Kantha and Tierney (1997). This is almost twice the 31 GW that Lien and Gregg (2001) estimated for global M_2 internal tide dissipation from an observed tidal beam and four times the 15 GW from the Hawaiian Ridge (Munk and Wunsch 1998; Egbert and Ray 2000). Combining our estimate with that of Lien and Gregg (2001) implies 89 GW or 25%–45% of the global internal tide dissipation is associated with shelf edge processes. Nash and Moum (2001) found 3×10^{-4} GW integrated over a 30 km^2 region at Stonewall Bank. Using an average shelf width of 60 km implies that small-scale shelf topography could account for up to 3 GW. The remainder is likely due to open-ocean topography such as ridges and seamounts.

Open-ocean thermocline mixing is an order of magnitude too low to account for the estimated 2.1 TW required to maintain abyssal stratification (Munk and Wunsch 1998). Rough topography is a likely candidate for generating the required mixing. Enhanced mixing in a canyon would mix deep water drawn up through the canyon axis with lighter surface water. A number of researchers have proposed that this water could be advected into the deep ocean along isopycnals and weaken the interior ocean stratification accounting for the large effective diffusivity (Armi 1978; Ivey and Nokes 1989; Munk and Wunsch 1998), although the mechanisms involved are not clear. Following Armi (1978), we calculate the effective global diapycnal diffusivity as

$$\overline{K_{\rho\,\text{global}}} \approx A_R \overline{K_{\rho\,\text{boundary}}}, \tag{6}$$

where A_r is the ratio of surface area associated with the boundary mixing to the surface area of the world's ocean (3.61×10^{14} m^2; Gill 1982) using $\overline{K_{\rho\,\text{boundary}}} = 1.3 \times 10^{-2}$ m^2 s^{-1} (section 3) with an associated surface area defined by 10% of the coastline and one-third of the shelf width. This would give an effective global diffusivity of 1.1×10^{-5} m^2 s^{-1} if canyon-related boundary mixing could affect the entire ocean.

b. Sampling resolution

One of our most surprising results was the lack of correspondence between regions of high dissipation and either S^2 or Ri^{-1} (Figs. 6, 9, and 10). In this section we speculate on two sampling issues that may have contributed to the observed lack of correspondence.

1) *Inadequate resolution of shear variance.* The 8-m vertical resolution of the ADCP may not be able to sufficiently resolve the shear variance at the scales where shear instabilities are developing. The Ozmidov scale, $L_O = \sqrt{\varepsilon/N^3}$, is the length scale where buoyancy forces equal inertial forces and is usually taken as an indication of the largest overturning scale. Using the average values observed in Monterey Canyon (1.1×10^{-6} W kg^{-1}, $N^2 = 6.8 \times 10^{-5}$ s^{-2}) give an overturning length of 1.4 m. The Thorpe scale (L_T) is the rms displacement of a particle in an overturn from its position in the corresponding stable water column. The distribution of observed Thorpe scales (Fig. 15a) shows that the majority are smaller than 1 m. Both these measures of overturning scales, the scales containing most of the turbulence, are small in comparison with the 8-m vertical resolution of the ADCP. Figures 15b,c show the Thorpe scale and the corresponding inferred dissipation values ($L_T N^3$, which assumes $L_T \approx L_O$) for the spring tide data averaged into 500-m along-axis bins. The spatial distribution of both L_T and $L_T^2 N^3$ as well as the magnitudes of $L_T^2 N^3$ are in good agreement with the measured dissipations (Fig. 6a), confirming the role of small overturns.

2) *Inadequate temporal resolution.* Although we averaged N^2 over the spatial bins before calculating Ri^{-1}, the drops cold have been from different tidal cycles and often only represented a fraction of the

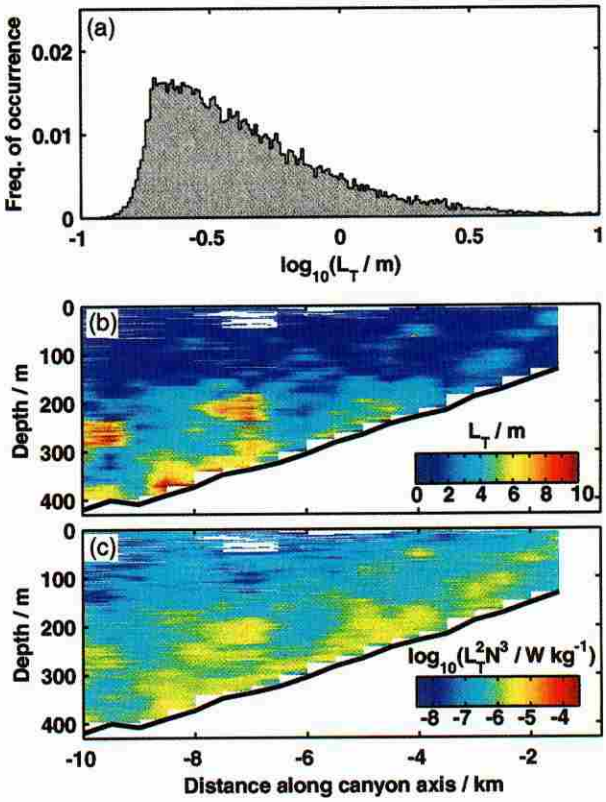

FIG. 15. (a) Distribution of Thorpe scales from all the data taken within 10 km of Moss Landing and within 250 m of the canyon axis, (b) Thorpe scales of spring tide data averaged into 500-m along-axis bins, and (c) dissipations inferred from Thorpe scales and stratification during spring tide. The inferred dissipations compare well with the measured dissipations plotted in Fig. 6a.

tidal cycle (e.g., Fig. 3). This averaging process may not have lend to an accurate description of the background stratification that the turbulence was acting on. In particular, if the background stratification was underestimated then $\mathrm{Ri}^{-1} = S^2/N^2$ would be biased high.

Unfortunately, we were unable to make the comparison in most of the STL (where the turbulence was highest) as ADCP velocities were not available that deep. The maximum depth for reliable ADCP velocities is governed by the first bottom reflection, normally the vertical sidelobe (RDI 1996), which results in the lowest 15% of the water column being discarded. However, with the ~15° sidewall slope observed in the cross-canyon survey, the first bottom reflection is off the sidewall from the sidelobe 60° from the vertical (30° beam angle). This leads to unreliable velocities in the lower 30% of the water column.

As this was the first microstructure survey near the head of a canyon, sampling was necessarily somewhat exploratory in nature. Energy fluxes, strain spectra, comparison with Ri^{-1}, and description of the pycnocline during the neap-relax density state all would have benefited from time series over at least a tidal cycle. However, fluxes and neap-relax dissipation were sensitive to canyon bends. Therefore future canyon studies need to balance spatial and temporal as well as vertical resolution considerations.

Acknowledgments. We are grateful to Jack Miller, Earl Krause, Gordy Welsh, Jen Mackinnon, Jody Klymak, Ren-Chieh Lien, and the crew of R/V *Point Sur*. Coastal Mixing and Optics data were kindly provided by Jen MacKinnon. Comments from Barbara Hickey, Chuck Nittrouer, Dave Winkel, Eric Kunze, Jen Mackinnon, Jeff Parsons, Jody Klymak, John Mickett, Jonathan Nash, Matthew Alford, and two anonymous reviewers have been helpful. This research was funded by the National Science Foundation Grant OCE9633067.

REFERENCES

Alford, M. H., and M. C. Gregg, 2001: Near-inertial mixing: Modulation of shear, strain and microstructure at low latitude. *J. Geophys. Res.*, **106** (C8), 16 947–16 968.

Armi, L., 1978: Some evidence for boundary mixing in the deep ocean. *J. Geophys. Res.*, **83** (C4), 1971–1979.

Bacon, S., L. R. Centurioni, and W. J. Gould, 2001: The evaluation of salinity measurements from PALACE floats. *J. Atmos. Oceanic Technol.*, **18,** 1258–1266.

Egbert, G. D., and R. D. Ray, 2000: Significant dissipation of tidal energy in the deep ocean inferred from satellite altimeter data. *Nature,* **405,** 775–778.

Ferron, B., H. Mercier, K. Speer, A. Gargett, and K. Polzin, 1998: Mixing in the Romanche Fracture Zone. *J. Phys. Oceanogr.*, **28,** 1929–1945.

Gardner, W. D., 1989: Periodic resuspension in Baltimore Canyon by focusing of internal waves. *J. Geophys. Res.*, **94** (12), 18 185–18 194.

Gargett, A. E., 1990: Do we really know how to scale the turbulent kinetic energy dissipation rate ε due to breaking of oceanic internal waves? *J. Geophys. Res.*, **95** (C9), 15 971–15 974.

Gill, A. E., 1982: *Atmosphere–Ocean Dynamics.* Academic Press, 662 pp.

Gordon, R. L., and N. F. Marshall, 1976: Submarine canyons: Internal wave traps? *Geophys. Res. Lett.*, **3,** 622–624.

Gregg, M. C., 1989: Scaling turbulent dissipation in the thermocline. *J. Geophys. Res.*, **94** (C7), 9686–9698.

——, 1998: Estimation and geography of diapycnal mixing in the stratified ocean. *Physical Processes in Lakes and Oceans,* J. Imberger, Ed., Coastal and Estuarine Studies, Vol. 54, Amer. Geophys. Union, 305–338.

——, and T. B. Sanford, 1988: The dependence of turbulent dissipation on stratification in a diffusively stable thermocline. *J. Geophys. Res.*, **93** (C10), 12 381–12 392.

——, and E. Kunze, 1991: Shear and strain in Santa Monica Basin. *J. Geophys. Res.*, **96** (C9), 16 709–16 719.

——, D. P. Winkel, T. B. Sanford, and H. Peters, 1996: Turbulence produced by internal waves in the oceanic thermocline at mid and low latitudes. *Dyn. Atmos. Oceans,* **24,** 1–14.

——, ——, J. A. Mackinnon, and R.-C. Lien, 1999: Mixing over shelves and slopes. *Dynamics of Oceanic Internal Gravity Waves II: Proc. 'Aha Huliko' a Hawaiian Winter Workshop,* Honolulu, HI, University of Hawaii at Manoa, 35–42.

Hickey, B. M., 1979: The California Current System—Hypothesis and facts. *Progress in Oceanography,* Vol. 8, Pergamon, 191–279.

——, 1995: Coastal submarine canyons. *Topographical Effects in the Ocean: Proc. 'Aha Huliko' a Hawaiian Winter Workshop,* P. Müller and D. Henderson, Eds. Honolulu, HI, University of Hawaii at Manoa, 95–110.

——, 1998: Coastal oceanography of western North America from the tip of Baja California to Vancouver Island. *The Sea,* A. R. Robinson and K. H. Brink, Eds., The Global Coastal Ocean, Vol. 11, John Wiley and Sons, 345–393.

Hotchkiss, F. S., and C. Wunsch, 1982: Internal waves in Hudson Canyon with possible geological implications. *Deep-Sea Res.*, **29,** 415–442.

Ivey, G. N., and R. I. Nokes, 1989: Vertical mixing due to the breaking of critical internal waves on sloping boundaries. *J. Fluid Mech.*, **204,** 479–500.

Kantha, L. H., and C. C. Tierney, 1997: Global baroclinic tides. *Progress in Oceanography,* Vol. 40, Pergamon, 163–178.

Key, S. A., 1999: Internal tidal bores in the Monterey Canyon. M.S. thesis, Dept. of Oceanography, Naval Postgraduate School, Monterey, CA, 91 pp.

Kunze, E., L. K. Rosenfeld, G. S. Carter, and M. C. Gregg, 2002: Internal waves in Monterey Submarine Canyon. *J. Phys. Oceanogr.*, **32,** 1890–1913.

Ledwell, J. R., A. J. Watson, and C. S. Law, 1993: Evidence for slow mixing across the pycnocline from an open-ocean tracer-release experiment. *Nature,* **364,** 701–703.

Lien, R.-C., and M. C. Gregg, 2001: Observations of turbulence in a tidal beam and across a coastal ridge. *J. Geophys. Res.*, **106** (C3), 4575–4591.

Lueck, R. G., and T. R. Osborn, 1985: Turbulence measurements in a submarine canyon. *Cont. Shelf Res.*, **4,** 681–698.

Moum, J. N., D. R. Caldwell, J. D. Nash, and G. D. Gunderson, 2002: Observations of boundary mixing over the continental slope. *J. Phys. Oceanogr.*, **32,** 2113–2130.

Munk, W., 1997: Once again: Once again—Tidal friction. *Progress in Oceanography,* Vol. 40, Pergamon, 7–35.

——, and C. Wunsch, 1998: Abyssal recipes II: Energetics of tidal and wind mixing. *Deep-Sea Res.*, **45,** 1977–2010.

Nash, J. D., and J. N. Moum, 2001: Internal hydraulic flows on the continental shelf: High drag states over a small bank. *J. Geophys. Res.*, **106** (C3), 4593–4611.

Oakey, N. S., 1982: Determination of the rate of dissipation of turbulent energy from simultaneous temperature and velocity shear microstructure measurements. *J. Phys. Oceanogr.*, **12,** 256–271.

Osborn, T. R., 1980: Estimates of the local rate of vertical diffusion from dissipation measurements. *J. Phys. Oceanogr.,* **10,** 83–89.

——, and W. R. Crawford, 1980: An airfoil probe for measuring turbulent velocity fluctuations in water. *Air–Sea Interaction: Instruments and Methods,* F. Dobson, L. Hasse, and R. Davis, Eds., Plenum Press, 369–386.

Percival, D. B., and A. T. Walden, 1993: *Spectral Analysis for Physical Applications: Multitaper and Conventional Univariate Techniques.* Cambridge University Press, 611 pp.

Petruncio, E. T., L. K. Rosenfeld, and J. D. Paduan, 1998: Observations of the internal tide in Monterey Canyon. *J. Phys. Oceanogr.,* **28,** 1873–1903.

Pickard, G. L., and W. J. Emery, 1990: *Descriptive Physical Oceanography: An Introduction.* 5th ed. Pergamon Press, 320 pp.

Polzin, K. L., J. M. Toole, and R. W. Schmitt, 1995: Finescale parameterizations of turbulent dissipation. *J. Phys. Oceanogr.,* **25,** 306–328.

——, K. G. Speer, J. M. Toole, and R. W. Schmitt, 1996: Intense mixing of Antartic Bottom Water in the equatorial Atlantic Ocean. *Nature,* **380,** 54–57.

RDI, 1996: *Acoustic Doppler Current Profiles: Principles of Operation—A Practical Primer.* 2d ed. RD Instruments, 51 pp.

Roemmich, D., S. Hautala, and D. Rudnick, 1996: Northward abyssal transport through the Samoan passage and adjacent regions. *J. Geophys. Res.,* **101** (C6), 14 039–14 055.

Rosenfeld, L. K., F. B. Schwing, N. Garfield, and D. E. Tracy, 1994: Bifurcating flow from an upwelling center: A cold water source for Monterey Bay. *Cont. Shelf Res.,* **14,** 931–964.

——, J. D. Paduan, E. T. Petruncio, and J. E. Goncalves, 1999: Numerical simulations and observations of the internal tide in a submarine canyon. *Dynamics of Oceanic Internal Gravity Waves II: Proc. 'Aha Huliko' a Hawaiian Winter Workshop,* P. Müller and D. Henderson, Eds. Honolulu, HI, University of Hawaii at Manoa, 63–71.

Slinn, D. N., and J. J. Riley, 1996: Turbulent mixing in the oceanic boundary layer caused by internal wave reflection from sloping terrain. *Dyn. Atmos. Oceans,* **24,** 51–62.

Thorpe, S. A., 2001: Internal wave reflection and scatter from sloping rough topography. *J. Phys. Oceanogr.,* **31,** 537–553.

Wesson, J. C., and M. C. Gregg, 1994: Mixing at Camarinal Sill in the Strait of Gibraltar. *J. Geophys. Res.,* **99,** 9847–9878.

Winkel, D. P., 1998: Influences of mean shear in the Florida Current on turbulent production by internal waves. Ph.D. thesis, University of Washington, 137 pp.

Wunsch, C., and S. Webb, 1979: The climatology of deep ocean internal waves. *J. Phys. Oceanogr.,* **9,** 235–243.

Copyright © 2002 EBSCO Publishing